24/12/2024 13:12

(Article begins on next page)

Understanding the Origin of Cycle-to-Cycle Variation using Large-Eddy Simulation: Similarities and Differences Between a Homogeneous Low-revving Speed Research Engine and a Production D.I. Turbocharged Engine

Abstract

A numerical study using Large-Eddy Simulations to reproduce and understand sources of cycle-to-cycle variation (CCV) in spark-initiated internal combustion engines (ICEs) is presented. Two relevantly different spark-ignition (S.I.) units, i.e. a homogeneous-charge slow-speed single-cylinder research unit (the TCC-III, Engine 1) and a stratified-charge high-revving speed GDI (Engine 2) one are analyzed in fired operations. Multiple-cycle simulations are carried out for both engines and LES results well reproduce the experimentally measured combustion CCV.

A correlation study is carried out, emphasizing the decisive influence of the early flame period variability (MFB1) on the entire combustion event in both ICEs. The focus is moved onto the early flame characteristics and the crucial task to determine the dominant causes of its variability (if any) is undertaken. A two-level analysis is carried out: the influence of global parameters is assessed at first; secondly, local details in the ignition region are analyzed. A comparison of conditions at combustion onset is carried out and case-specific leading factors for combustion CCV are identified and ranked.

Finally, comparative simulations are presented using a simpler flame deposition ignition model: the simulation flaws are evident due to modelling assumptions in the flame/flow interaction at ignition.

The relevance of this study is the knowledge extension of turbulence-driven phenomena in ICEs allowed by advanced CFD simulations. The application to different engine types proves the soundness of the used models and it confirms that CCV is based on engine-specific factors. Simulations show how CCV originates from the interplay of small- and large-scale factors in Engine 1, due to the lack of coherent flows, whereas in Engine 2 the dominant CCV promoters are local AFR and flow velocity at ignition. This confirms the absence of a generally valid ranking and it demonstrates the use of LES as a development and design-orienting tool for next-generation engines.

Introduction

Cyclic variation in S.I. engines is the undesired degree of non-repeatability of consecutive combustion events when operating under nominally stationary conditions (e.g. same load, rpm, manifold absolute pressure, etc.). This is ultimately caused by the turbulent nature of engine flows, whose randomic and unsteady structures are the environment for in-cylinder processes (e.g. mixture formation and combustion development). Combustion irregularity leads to reduced thermal efficiency (e.g. late spark-timing to avoid sporadic knock), increased pollutants emission (e.g. due to incomplete combustion) and fuel consumption. The urgency to understand the origin of CCV emerges as a first-order research guideline for applied combustion research. The topic has been extensively described in literature, with exhaustive reviews as in [1, 2]. In particular, Finney et al. in [3] confirm the lack of governing effects valid for all the S.I. engines for

operating conditions within the stable portion of the engine map, though the relevance of deterministic and controllable factors is expected to emerge with the interest in fuel-saving unstable operations. This enforces the need to develop and validate CFD models able to directly handle the underlying physics with the minimum set of assumptions.

Large-Eddy Simulation is a well-established analysis tool to simulate combustion CCV [4, 5], thanks to the capability to capture the unsteadiness of large-scale turbulent flows while relying on sub-models for small-scale turbulence modelling. As for these last, both simple (e.g. the dissipative Smagorinsky [6]) and advanced (e.g. the one-equation Dynamic [7] or WALE [8]) models have been widely used in numerical studies. In [9, 10] Ko et al. compared simple and advanced subgrid-scale models in the same TCC engine studied in this paper, operated under motored conditions; a comparison with PIV acquisitions was presented. Results showed that the dissipative-only nature of the Smagorinsky model can adequately reproduce both mean flow structures and their variability if a dynamic formulation of model constant c_s (linked to subgrid-scale eddy-viscosity) is adopted. Other compared PIV and LES studies on the motored TCC engine can be found in [11-13]. In [14] Goryntsev et al. showed the effect of the superimposition of flow and mixture variability on an optically-accessible direct injection engine. The isolation of individual contributions made possible by LES allowed the authors to understand the individual role of each factor, otherwise difficult to discern due to their simultaneous occurrence; LES was then used to study the misfire tendency in [15]. On the same research engine LES was used by Janas et al. [16] to describe the evolution of the flow field from intake flow through valves to tumble break-down and the comparison between turbulence models by Buhl [17] and by Nguyen et al. [18] confirmed the suitability of the adopted LES models to understand the turbulent flow structures in ICEs.

Local flows in the spark-plug surroundings and global/local air-to-fuel ratio (AFR) at ignition are commonly identified as the main responsibles for CCV, as reported in [19-21], in the review on EGR strategies by Wei et al. [22] and in LES-based investigations [23-26]. However, a unique rank of CCV-governing factors is not generally proposed, due to the wide variety of layouts and operations of S.I. engines (i.e. premix/direct-injected, port orientation, number of valves, valve actuation strategies, etc.). The relative/mutual influence of all these factors is still unclear, probably depicting the absence of universal dominant factors valid for any kind of S.I. engine/operation. This strengthens the need of physics-based numerical models for spark-ignition and flame propagation, able to simulate the combustion behaviour of S.I. engines depending on local physical aspects only, with a minimum set of modelling assumptions. In this study the ISSIM-LES ignition model [27] is adopted, fulfilling all the mentioned requirements for flame kernel development simulation. The model was motivated by the possibility to use the same Flame Surface Density equation (FSD-LES) as for flame propagation in the ECFM-LES combustion model also for initial flame kernel, provided that dedicated terms were added for additional subgrid-scale flame contributions at ignition. Robert et al. in [28] improved the ISSIM-LES model and they used LES to simulate the cycle-dependent knock occurrence in a small S.I. engine. LES was also used by Pan et al. in [29] coupled with a detailed chemistry solver to simulate the knock occurrence of a downsized S.I. engine and the cycle-dependent developing detonation transition.

An initial attempt for pondering the effect of spark-plug geometry on CCV was presented by Fontanesi et al. [30], although a simple flame deposition model was used for spark-ignition. In [31-33] d'Adamo et al. showed the early application of ISSIM-LES in the STAR-CD CFD code. In [34] the TCC engine was first studied under fired conditions, comparing two combustion models (ECFM-LES [35, 36] and Thickened Flame Model [37, 38]) and using optical diagnostics to correlate flow variability at spark with combustion CCV. The relevance of the early 1% of Mass Fraction Burnt (MFB) duration was found to be a leading parameter for the entire combustion event, and flame visualizations allowed to compensate the poor-resolution of pressure-based analysis at the very initial stage. Optical diagnosis from [39] was used to clarify

the dominant factors for CCV, thus ranking first- and second-order processes leading to combustion irregularity.

In this paper the numerical models used in previous studies are applied to two largely different S.I. engine configurations. The aim is to demonstrate the robustness and universality of the numerical models, with focus on spark-ignition and flame nucleus growth. Pressure-based experimental data are used to quantitatively assess the degree of simulated CCV; later, correlation analysis is used to highlight the relationship between easily measurable combustion variables (i.e. maximum pressure) and early flame period duration. Simulations are used to investigate the role of both large-scale factors and local flow details in the proximity of spark plug in promoting combustion CCV. The multiple differences in the two S.I. units lead to non-unique conclusions for governing reasons of CCV. The different description of flow/flame interplay using a unique spark-ignition model (ISSIM-LES) confirms the capability to simulate the engine-specific factors leading to CCV. The role played by the ignition model is further emphasized by the unsatisfactory results obtained when substituting it with a simpler flame deposition model.

The outcomes obtained by the analysis on two largely different S.I. engines suggest that factors leading to CCV can only be identified for individually studied ICEs and not for all types of engines, in agreement with the relevant body of literature on the topic. This study demonstrates how this knowledge limitation can be overcome by the unprecedented understanding given by CFD analyses, paving the way for the extensive application of LES simulations in the design and development of future ICEs.

Investigated Engines

The two S.I. units analyzed in this study are chosen to represent largely different configurations for spark-initiated combustion engines. The first unit (Engine 1) is the well-known TCC-III single-cylinder 2-valve research engine with transparent combustion chamber operated by University of Michigan and GM. The engine is illustrated in Figure 1. The pancake-shaped engine was designed to provide simulation-tailored experiments to investigate engine flows and it has been largely used to develop and validate numerical models for both turbulence and combustion, as introduced in the previous section. Considering firing conditions, a detailed description of both experiments and simulations can be found in [39] for diluted/stoichiometric mixtures of several fuels. The experimental data collection consists of 358 consecutive cycles and it is publicly available in [40]. The operating condition analyzed in this study is a 1300 rpm premixed stoichiometric propane-air operation, with MAP (Manifold Absolute Pressure) equal to 40 kPa and SA=18 CA bTDC. For such operating condition, a first simulation study in [34] showed the relevance for MFB1 duration for this engine/operation.
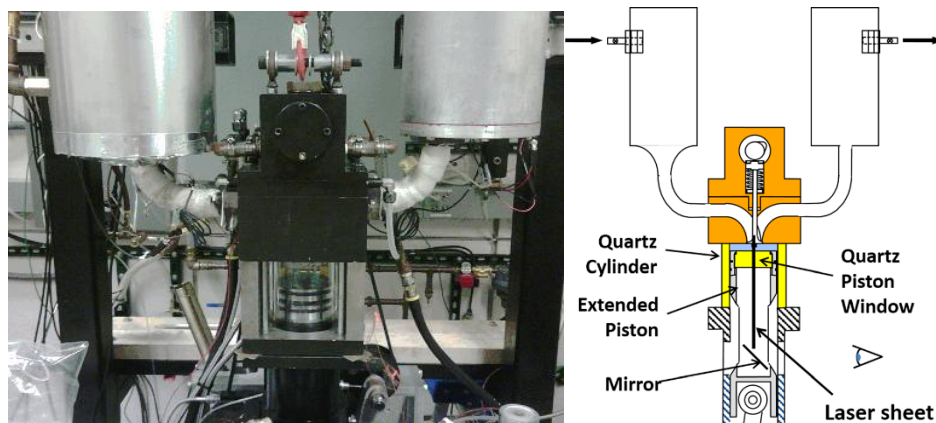

Figure 1. The TCC-III single-cylinder engine apparatus (left, from https://deepblue.lib.umich.edu/data/) and sketch (right, from [39]).

The second unit (Engine 2) is a 4-valve production turbocharged GDI engine, whose analyzed condition is the peak-power 7000 rpm one. For this operation a direct-injected fuel-enriched (Equivalence Ratio=1.3) fuel/air mixture is created through a 7-hole side-mounted injector. Fuel-enrichment is commonly adopted in knock-limited S.I. engines to reduce the knock tendency, due to the benefit in specific heat of over-fuelled mixtures as reported by Vafamehr et al. [41]. This unit was analyzed by the authors in previous papers [30-33] as representative of a modern production unit with high-end specific power; in the analyzed dataset 240 knock-limited cycles are measured. The fuel used in the experiments is a commercial RON98-E0 unleaded gasoline. The main geometrical dimensions and test bench data are reported in Table 1 for both units.

	Engine 1 (TCC-III)	Engine 2 (GDI Turbocharged)
Bore / Stroke [mm]	92 / 86	86.5 / 80.8
Geometrical Compression Ratio	10	9.6
Conn. Rod Length [mm]	231	141.25
Revving Speed [rpm]	1300	7000
Valves per cylinder	2	4
Fuel	Propane	Gasoline (RON98-E0)
Fuel/Air Equivalence Ratio	1.0 (premixed)	1.3 (stratified charge)
Spark Timing [CA bTDC]	18	12
Electrical Ignition Energy [mJ]	36.5	85
Electrode Gap [mm]	1.15	0.9

Table 1. Main geometrical and operation parameters for Engine 1 and 2.

Numerical Models

Numerical simulations are carried out on two models reproducing a full cylinder and part of the intake/exhaust lines for each engine; moreover, the two sets of simulations share as many sub-models as possible in order to coherently compare the two sets of CFD results.

Engine 1 is reproduced considering both the intake and exhaust plenums. The total number of cells is approx. 1M/600k at BDC/TDC, with an average cell size of 0.8 mm. A refinement block is added around the fully meshed spark plug, with a local cell size of 0.5 mm. Engine 2 is simulated from the in-head portion of the intake port to the turbine inlet section of the exhaust line, for a total of 2M/1.1M cells at BDC/TDC. The mean cell size is 0.7 mm with a refinement block of 0.3 mm cell size in the spark plug region. A view of the cylinder region for the two engines is reported in Figure 2, where a section plane is used to show the grid details in proximity of the fully meshed spark plugs.
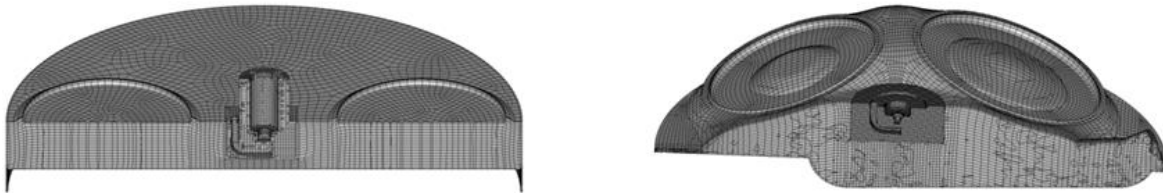
Figure 2. Section view of grid at TDC for Engine 1 (left) and Engine 2 (right).

A set of 60 consecutive engine cycles is simulated for Engine 1, whereas 23 cycles are calculated for Engine 2. All the simulations are carried out using the CFD code STAR-CD v4.28 licensed by SIEMENS PLM. The same numerical schemes for discretization are adopted for both engines, i.e. 2nd order for momentum, energy and transported scalars. The used scheme for all variables is the Monotonic Advection Reconstruction Scheme (MARS), which is based on a multidimensional Total Variation Diminishing (TVD) method [42]. In

both models the subgrid-scale turbulence is modelled using the Smagorinsky model, with constant c_s value equal to 0.202. Boundary conditions are imposed as time-varying pressure-temperature signals at inlet/outlet sections. These are derived from experimental cycles-resolved acquisitions: for both the engines a negligible cyclic variation of (p,T) was measured, hence a periodic ensemble-average pressure profile is used as boundary condition [43]. Wall temperatures are imposed as region-specific values in both engines, whose thermal level is derived by tuned 1-D models of both units. Wall heat transfer is simulated using the developed GruMo-UniMORE Wall Function [44, 45], allowing a predictive heat rejection budget thanks to the use of an alternative thermal law of the wall. In the RANS context it improved the predicted gas-to-wall heat transfer even for highly-charged S.I. engines, for which commonly adopted models are known to relevantly overestimate the transferred heat. The application of this model in the LES context is motivated by the solid physical basis and following the verification that the same amount of thermal power is overall exchanged between RANS and LES simulations of the same engines. The near wall grid is purposely calibrated to guarantee a proper estimation of gas-to-wall fluxes, as described in [46].

While Engine 1 operates with a homogeneous propane/air mixture, Engine 2 needs a dedicated treatment for the direct injection of gasoline. This is modelled using a Lagrangian approach for the liquid spray of the 7-hole gasoline injector. To reproduce the primary break-up of the liquid fuel injection (100 bar injection pressure) a calibrated set of Rosin-Rammler distributions of discrete parcels is introduced at each time step during injection [47-49] to meet individual spray plume penetration, droplet size, diameter distribution and spray momentum [50]. The interaction with in-cylinder turbulent flows leads to spray secondary break-up, accounted for by Reitz sub-model [51], forming a partially-premixed charge directed in the spark-plug region by the piston asymmetric shape visible in Figure 2.

Combustion is modelled using the ECFM-LES model, where flame surface density evolution is reproduced by the transport equation first proposed in [35, 36] accounting for subgrid/resolved contributions on FSD-LES. In this study a modified FSD-LES equation (Eq. 1) is used to consider the subgrid-level contribution at spark-ignition, where T_{res}, T_{sgs}, C_{res}, C_{sgs}, S_{res} and S_{sgs} are the resolved and subgrid-scale contributions to $\bar{\Sigma}_{\tilde{c}}$ transport, curvature and stretch, respectively, while $\dot{\omega}_{\Sigma}^{ign}$ is the source term from ignition. This is the fundamental concept of the ISSIM-LES ignition model [27], where the theoretical capability of the FSD-LES transport equation to describe the coherent flame evolution since the early stage is exploited. A modification is needed due to the flame stretch at subgrid-scale for small-radii flames (i.e. at ignition), whose effect is considered by the $S_{ign} = \frac{2}{3}\frac{(1+\tau)}{\tilde{c}} s_L \bar{\Sigma}_{\tilde{c}}$ term (with $\tau = {T_b}/{T_u} - 1$). A transition function of the filtered flame radius r_b^+ (with $r_b^+ = r_b / \widehat{\Delta}$, being $\widehat{\Delta}$ the mean cell size used as filter length for turbulence) is used to govern the continuous evolution to a fully-resolved propagating flame. To this aim the adopted $\alpha(r_b^+)$ function is reported in Eq. 2.

$$\frac{\partial \bar{\Sigma}_{\tilde{c}}}{\partial t} = T_{res} + T_{sgs} + S_{sgs} + \alpha C_{sgs} - \nabla \cdot \left(\alpha S_d N \overline{\Sigma}_{\tilde{c}} \right) + \alpha(C_{res} + S_{res}) + (1 - \alpha)S_{ign} + \dot{\omega}_{\Sigma}^{ign} \qquad \text{(Eq. 1)}$$

$$\alpha = 0.5 \left[1 + tanh\left(\frac{r_b^+ - 0.75}{0.15} \right) \right] \qquad \text{(Eq. 2)}$$

In the limit of $r_b^+ \to \infty$, $\alpha(r_b^+) \to 1$ and the standard FSD-LES equation is restored by suppression of the S_{ign} term. The subgrid-scale wrinkling factor proposed by Robert et al. [28] is introduced in the model (Eq. 1): it is derived considering the analytical wrinkling of a spherical flame $\Xi = r_b \bar{\Sigma}_{\tilde{c}} / (3 \cdot \tau)$ and overcoming the assumption $\Xi = 1$ present in the original formulation [27], thus leading to the correct $\frac{2}{3}\frac{(1+\tau)}{\tilde{c}} s_L \bar{\Sigma}_{\tilde{c}}$ expression. A simplified sub-model of the secondary electric circuit is present from Duclos et al. [52], considering the spark-to-gas energy transfer during the glow phase and calculating a discharge duration from this budget. The model is based on Verhoeven's measurements [53], indicating 60% efficiency for energy

transfer. The flame kernel is initialized as the equivalent burnt mass of a cylinder with radius $2\delta_L$ and height equal to the electrode distance (see Table 1).

Laminar flame speed (LFS) is modelled in both engines using a developed methodology based on detailed chemistry simulations of unstretched freely propagating flames at engine conditions. The rationale is presented in [54, 55] and it is here briefly resumed for the sake of clarity. Pressure and temperature levels typical of engine flames are considered to simulate the structure of unstretched laminar flames. Once a consistent set of LFS is obtained as a function on the equivalence ratio ϕ, a fitting procedure using MATLAB is carried out to obtain the a_i, b_i and c_i ($i = 0, ...,5$) coefficients to close the polynomial power-law in Eq. 3. The reference pressure and temperature (p_0, T_0) and a_i, b_i and c_i coefficients for each fuel are reported in Appendix.

$$s_L = \left[\sum_{i=0}^{5} a_i \cdot log\,(\phi)^i\right] \cdot \left(\frac{T}{T_0}\right)^{\sum_{i=0}^{5} b_i \cdot log\,(\phi)^i} \cdot \left(\frac{p}{p_0}\right)^{\sum_{i=0}^{5} c_i \cdot log\,(\phi)^i} \tag{Eq. 3}$$

This method allows the use of a CPU-efficient algebraic correlation (i.e. no chemical reactions solved during the CFD run) preserving the fidelity of detailed chemistry simulations. While for Engine 1 the fuel composition known (pure propane, for which the mechanisms from Ranzi et al. [56] and by Qin et al. [57] is used for LFS simulations), the commercial RON98-E0 Gasoline used in Engine 2 is reproduced by a ternary surrogate composed by 56/28/17% mol.% of iso-octane/toluene/n-heptane following the blend proposed by Gauthier et al. in [58] and using the chemical mechanism by Andrae et al. [59, 60].

Calculation times needed for full-cycle simulations including combustion on a 48-cpu HPC cluster are in the order of 48 hours for Engine 1 and 96 hours for Engine 2. As for this last, the higher number of cells needed to model the complex geometric combustion chamber sums to the reduced time-steps needed to preserve the CFL number below unity during high-velocity fuel injection, leading to an almost double CPU time. This motivates the lower number of simulated cycles for Engine 2 (23) with respect to Engine 1 (60); for both engines the first 2 complete LES cycles were discarded to cancel the effect of flow initialization on the analyzed solution. An efficient strategy to reduce the overall time needed for these analyses and bridge LES simulations to the standard industrial development is the Parallel Perturbation Model (PPM) proposed by Ameen et al. in [61], which proved able to separate long time-scale CCV into several short time-scale simulations, effectively reproducing the same degree of cyclic variability.

Finally, the quality of LES results obtained on the adopted grids is evaluated using the Energy Resolution (ER) parameter first introduced by Pope in [62] (Eq. 4), stating that a sufficient quality is achieved if a minimum of 80% of the total kinetic energy ($K_{tot} = K_{res} + K_{sgs}$) is resolved with the filtered momentum equations (K_{res}) and not modelled at subgrid scale (K_{sgs}):

$$ER = \frac{K_{res}}{K_{res} + K_{sgs}} \tag{Eq. 4}$$

The quality of the filtered flow fields was assessed by Ko et al. in [63] for Engine 1 under motored conditions: as for fired operations, analogous considerations can be undertaken as shown in [34, 38], where the average flow fields were obtained in PIV and LES on two cutting planes both under motored and fired conditions. A similar analysis based on the kinetic energy fraction modelled at subgrid-scale was carried out in [31, 32], confirming the adequacy of the grid used for Engine 2 simulations.

Simulation Results

Cycle-resolved combustion traces are reported in Figure 3 for both experiments and LES simulations, together with the burnt fraction calculated from the analysis of the cycle-resolved Rate of Heat Release (ROHR). These last are re-calculated from the pressure trace and the in-cylinder volume, so that the same calculation procedure is adopted for both experiments and simulations. The ROHR is obtained as in Eq. 4, and the cumulative heat release (CHR) for each cycle is integrated in Eq. 5. Finally, the burnt fraction is normalized on the maximum CHR for each cycle to obtain the apparent Mass Fraction Burnt (aMFB).

$$ROHR = \frac{\gamma}{\gamma-1} \cdot p \cdot \frac{dV}{dt} + \frac{1}{\gamma-1} \cdot V \cdot \frac{dp}{dt} \qquad \text{(Eq. 4)}$$

$$CHR = \int \ ROHR \cdot dt \qquad \text{(Eq. 5)}$$

In Eq. 4 γ is the ratio of specific heats ($\gamma = c_p/c_v$); the ROHR and apparent mass fraction burnt (aMFB) calculations are carried out from -20 CA aTDC to +60 CA aTDC. The same method is shared between experiments and simulations for both Engine 1 and 2 to carry out coherent comparisons. In Figure 4 the cycle-dependent peak pressure location and its phasing in the cycle is shown for both experiments and simulations, showing an overestimation of combustion CCV for Engine 1 while an excellent result is obtained for Engine 2.
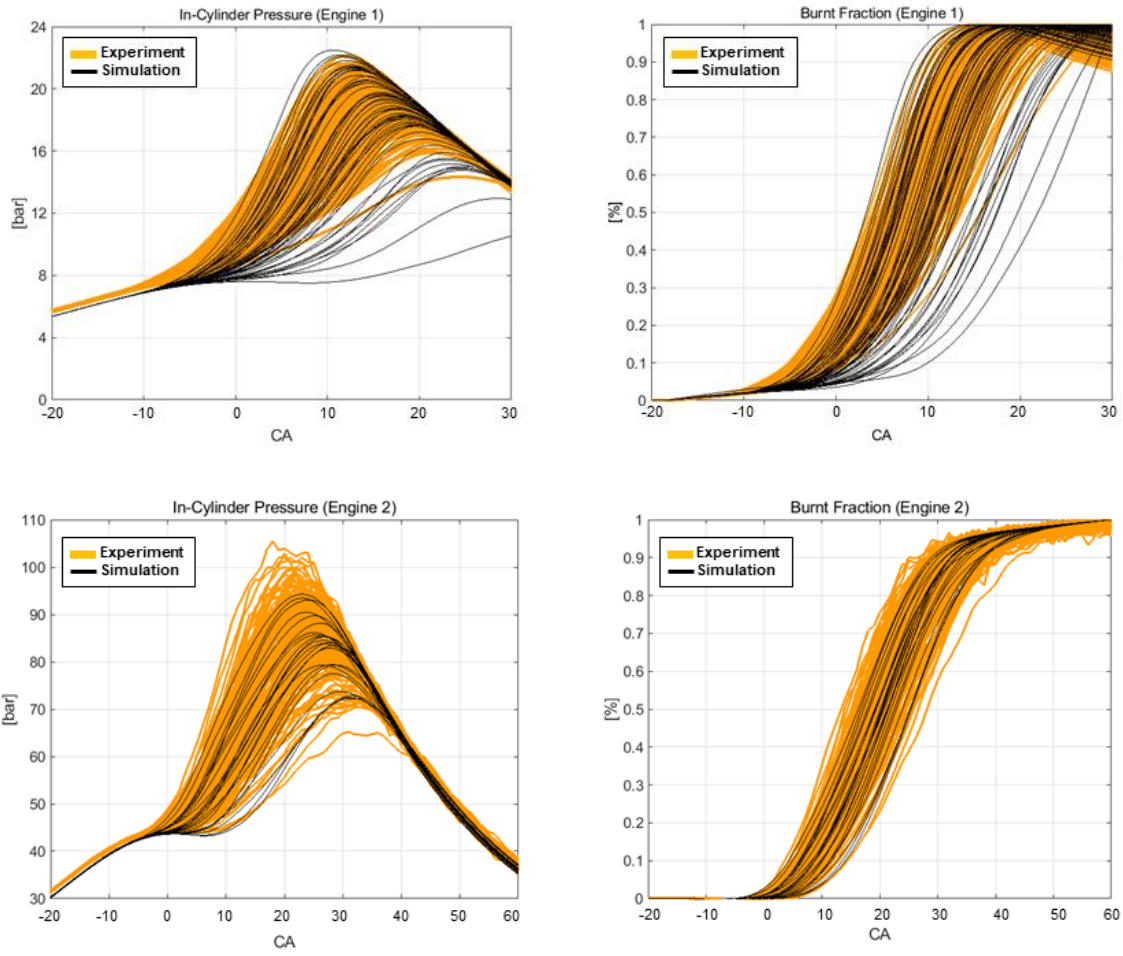

Figure 3. In-cylinder combustion (left side) and burnt fraction (right side) of Engine 1 (top row) and Engine 2 (bottom row) for experiments (orange lines) and simulation (black lines).
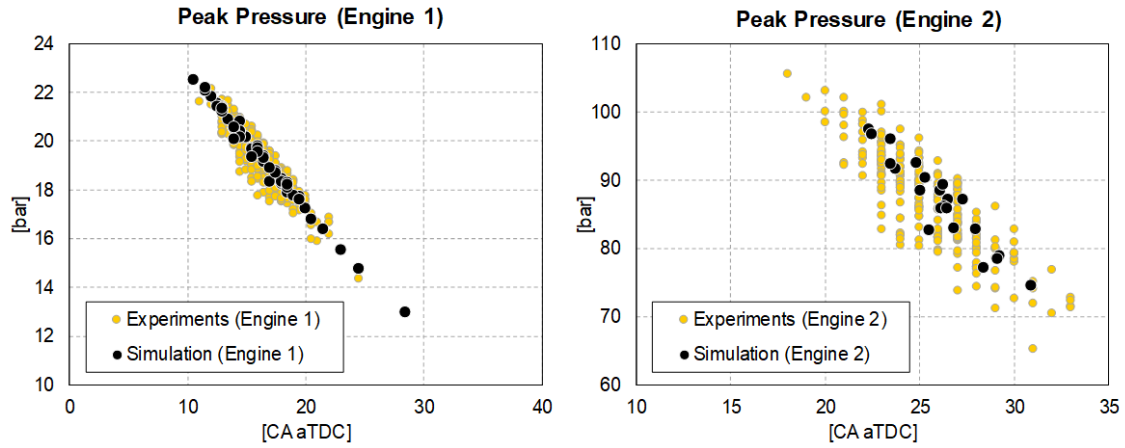
7

Figure 4. Peak pressure value and phasing for experiments and simulation: Engine 1 (left) and Engine 2 (right).

As visible from Fig.3, Engine 1 simulations suffer from a pressure underestimation during the compression stroke: this effect is present also in the 1D model of the engine and will be amended in the near future. This is also present (to a minor extent) in Engine 2. However, to the aim of the burn rate analysis and simulated CCV, this is not considered as a factor altering the object of the study (i.e. the interplay of turbulence/flow/combustion); therefore, the present simulations are used to understand the origin of CCV. The assessment of statistical convergence of the simulated dataset (i.e. 60 samples for Engine 1, 23 samples for Engine 2) is conducted by calculating the evolution of the average and RMS values of peak pressure. The simulated combustion cycles are in good agreement with the experimental ones considering the average peak pressure for both engines, while p_{max} RMS is overestimated in Engine 1. For such engine, some slow-burning cycles are present in the simulated dataset which are not detected by experiments (Figure 3, top row), hence overestimating the CCV in the slower-than-average burn rate band. Both engines reach a good stability of the average and RMS p_{max} values in the limit of the number of simulated cycles, as shown in Figure 5 for both experiments and simulations: in particular, statistics on experimental values calculated on the same number of cycles as simulations are very close to the values obtained for the complete dataset. In Table 2 mean, RMS and CoV values are reported for peak pressure, the CA of peak pressure (CA p_{max}), IMEP (calculated in the combustion window) and the aMFB50 phasing. The coefficient of variation (CoV) in Table 2 is calculated as the percentage ratio of the RMS to the mean value. Therefore, the available datasets are considered as representative of combustion CCV for both engines and simulations will be used to understand the origin of CCV in the two units.

	Engine 1		Engine 2	
Variable	**Experiments**	**Simulation**	**Experiments**	**Simulation**
Peak Pressure Aver. [bar]	19.2	19.3	87.0	86.9
Peak Pressure RMS [bar]	1.1	1.9	7.1	6.3
Peak Pressure CoV [%]	5.7%	9.8%	8.1%	7.2%
CA p_{max} Aver. [CA aTDC]	16.4	17.5	25.5	26.1
CA p_{max} RMS [CA]	1.93	4.4	2.7	2.2
CA p_{max} CoV [%]	11.8%	25.4%	10.4%	8.5%
IMEP Aver. [bar] Engine 1 range: [-18;+60] CA aTDC Engine 2 range: [-12;+60] CA aTDC	5.0	4.9	49.3	48.9
IMEP RMS [bar]	0.14	0.5	2.2	2.6
IMEP CoV [%]	2.8%	9.5%	4.4%	5.3%
aMFB50 Aver. [CA aTDC]	8.3	10.4	20.1	20.8
aMFB50 RMS [CA]	1.9	4.3	2.5	2.6
aMFB50 CoV [%]	22.4%	41.8%	12.6%	12.7%

Table 2. Measured average, root mean square deviation and calculated CoV of peak pressure, crank angle of peak pressure, IMEP and aMFB50 for Engine 1 and 2.
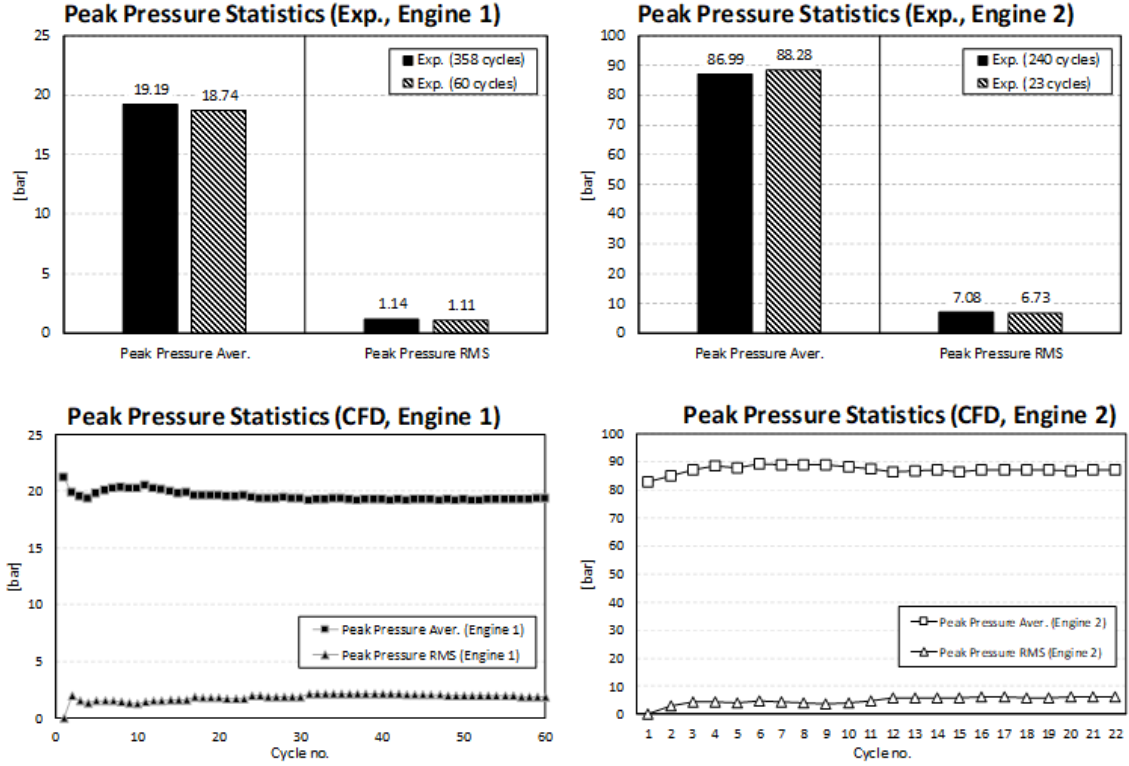
Figure 5. Convergence of statistics (ensemble average and RMS) for peak pressure of Engine 1 and 2. Top: experiments; bottom: simulations.

Analysis of Combustion Indicators

Consistently with the common experimental practice, the analysis of the pressure trace can be used also to calculate the apparent combustion indicators (e.g. aMFB10, aMFB50, etc.) from simulations. The search for leading factors for combustion variability is pursued using the most common metrics used in the experiments: the variability of the peak pressure (p_{max}) is observed, and correlation analysis is used to identify relationships between phasing indicators and combustion CCV. To this aim the Pearson Correlation Coefficient ρ_{XY} is used to quantify the link between the variation of X-variable to the one of Y-variable, using the standard deviations of X and Y variables (σ_X and σ_Y) and the covariance of X and Y (σ_{XY}) as in (Eq. 6):

$$\rho_{XY} = \frac{\sigma_{XY}}{\sigma_X \sigma_Y} \qquad\qquad\qquad\qquad \text{(Eq. 6)}$$

The good correlation between simulation and experiments is illustrated in Figure 6 in terms of aMFB10/aMFB50 relationship with peak pressure: as for Engine 1 $\rho_{pmax\text{-}aMFB10}$=-0.82/-0.97 (exp./sim.) and $\rho_{pmax\text{-}aMFB50}$=-0.89/-0.99 (exp./sim.), with an initial combustion phasing delay probably due to pressure underestimation at ignition, while for Engine 2 $\rho_{pmax\text{-}aMFB10}$=-0.88/-0.91 (exp./sim.) and $\rho_{pmax\text{-}aMFB50}$=-0.97/-0.98 (exp./sim.). However, this close relationship is poorly explanatory on the root causes for combustion CCV, as the flame is well developed at this stage and it prevents to ponder the effect of local and large-scale factors on combustion onset and development
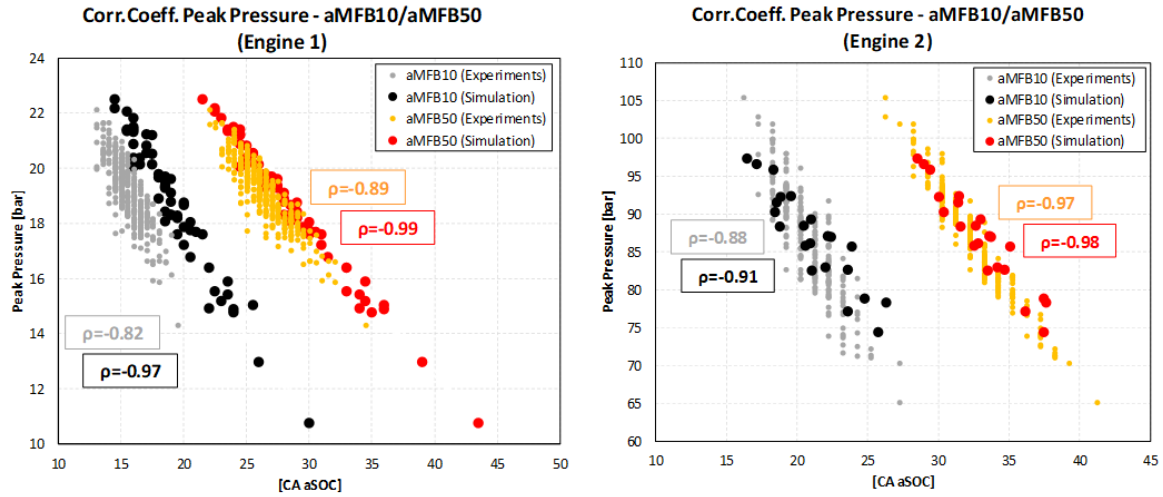
Figure 6. Correlation between aMFB10/aMFB50 and peak pressure for experiments and simulations: Engine 1 (left) and Engine 2 (right).

To overcome this limitation, the numeric heat release rate is considered to calculate the MFB indicators. This allows to circumvent the issues related to pressure trace analysis during the very early stages of flame growth and development: the analysis based on the experimental pressure signal would be severely affected by the low signal-to-noise ratio due to the negligible heat released at such stage. Simulations can therefore be used to extend the comprehension of physical phenomena.

A well-established strong correlation is confirmed between the variability of p_{max} and that of MFB50, as reported in Figure 7: this is confirmed as high as $\rho_{pmax-MFB50}=1.00$ and $\rho_{pmax-MFB50}=0.98$ for Engine 1 and 2, respectively. The same correlation analysis is backwards repeated for the CCV of MFB10, MFB5 and MFB1 with p_{max}; strong relationships with early combustion phasing are found for both engines back to MFB1 ($\rho_{pmax-MFB10}=0.96$ for Engine 1 and $\rho_{pmax-MFB10}=0.90$ for Engine 2), as reported in Figure 7. This states that most of the combustion CCV is originated in-within the first 1% of fuel burnt fraction (MFB1). Simulations are then used to quantify the impact of large-scale and local phenomena acting on the growing flame kernel; in the next section the study will focus on the effects of simulated large-scale and small-scale variables on combustion development.
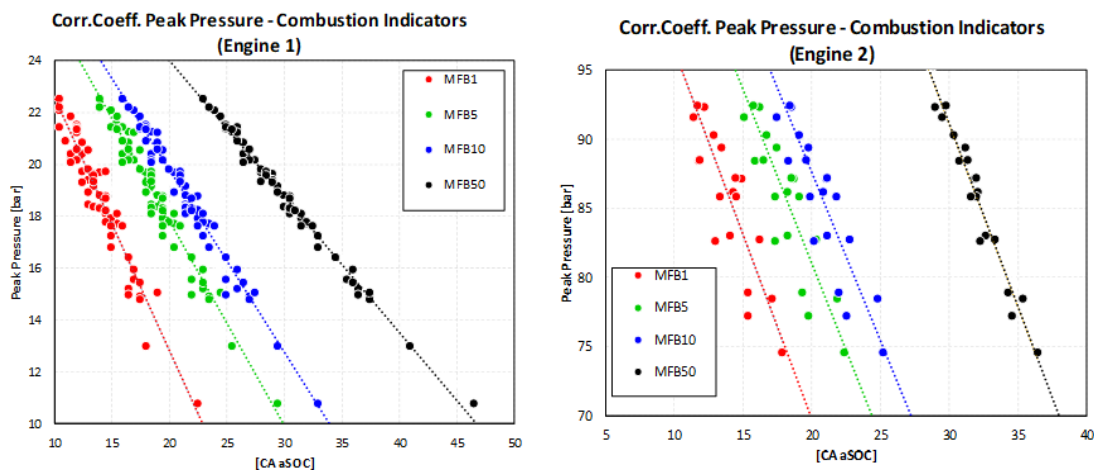

Figure 7. Correlation analysis between combustion indicators (MFB50, MFB10, MFB5, MFB1) and peak pressure for Engine 1 and 2.

Analysis of Large-Scale Variables on Combustion Variability

Initial candidate large-scale factors for combustion cyclic variability of MFB1 are the mean in-cylinder pressure and temperature levels at ignition time (Figure 8). In this analysis, values at ignition time for both engines are considered, i.e. 18 CA bTDC for Engine 1 and 12 CA bTDC for Engine 2 (see Table 1): this

10

allows to accurately analyse flow conditions at combustion onset. However, combustion CCV of both engines shows a very reduced correlation with temperature (ρ_{T-MFB1}=0.12 for Engine 1 and ρ_{T-MFB1}=0.06 for Engine 2); as for pressure, a similar result is confirmed for Engine 1 (ρ_{p-MFB1}=0.04), while Engine 2 exhibits a moderately higher value of ρ_{p-MFB1}=0.33. Moving to the effect of in-cylinder trapped quantities, the variability of trapped gas mass, vapour fuel mass and the dilution rate is then correlated to the MFB1 cyclic variation. As visible in Figure 9, the trapped mass of gas and of vapour fuel shows an expected negligible impact on MFB1 for the premixed-operated Engine 1 ($\rho_{mass-MFB1}$=0.02 and $\rho_{Fuel-MFB1}$=0.07, respectively), while in Engine 2 a non-negligible relationship holds ($\rho_{mass-MFB1}$=0.21 and $\rho_{Fuel-MFB1}$=0.24, respectively). This last factor is associated to the mentioned sensitivity on pressure for Engine 2 (ρ_{p-MFB1}=0.33), stating a mixture quality variation dependence on trapped gas mass and in-cylinder pressure.

The charge dilution in both engines is only due to internal recirculation of burnt products, as external EGR is not adopted in Engine 1 or in Engine 2. The analysis of dilution rate at ignition well agrees between the two engines, with $\rho_{EGR-MFB1}$=-0.05 and $\rho_{EGR-MFB1}$=-0.01 for Engine 1 and 2, discarding this as a responsible factor for combustion CCV.
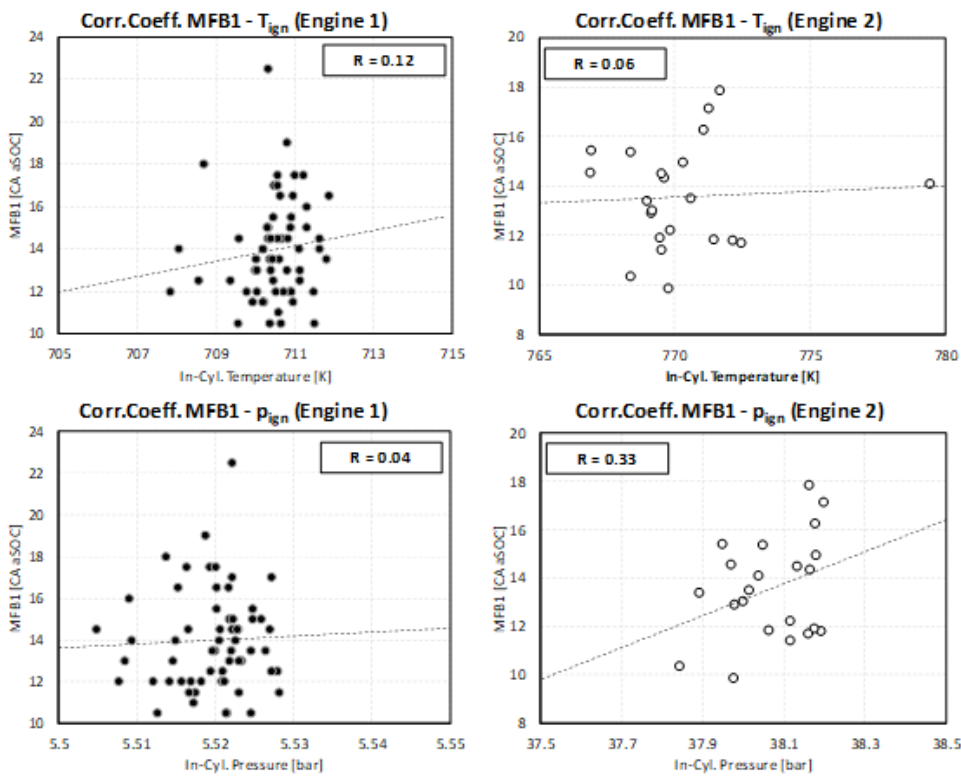

Figure 8. Correlation analysis between in-cylinder temperature (top row)/pressure (bottom row) at ignition and MFB1 combustion duration for Engine 1 (left side) and 2 (right side).
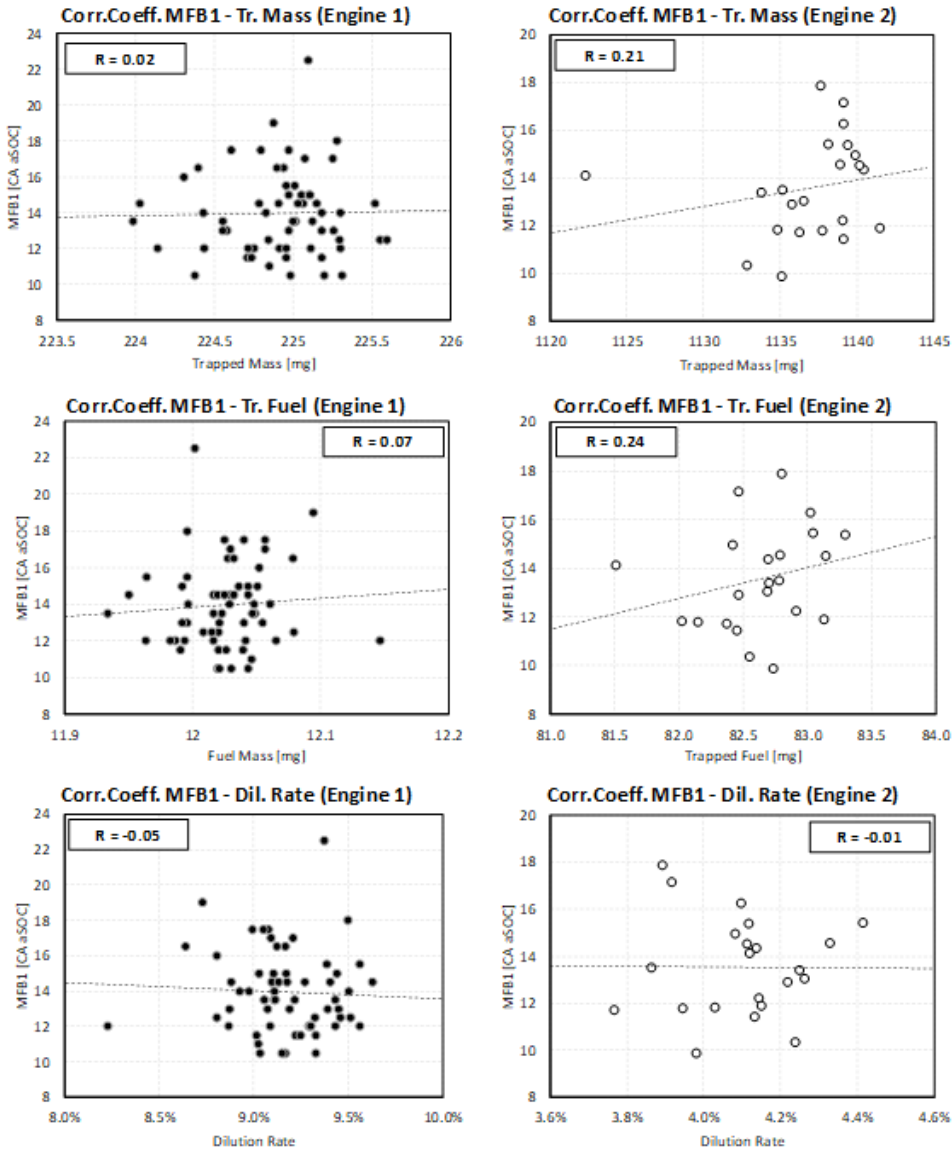
Figure 9. Correlation analysis between trapped gas mass (top row)/trapped fuel (middle row)/dilution rate (bottom row) at ignition and MFB1 combustion duration for Engine 1 (left side) and 2 (right side).

Finally, the analysis moves to the global characteristics of the in-cylinder flow field, i.e. the intensity of coherent tumble, swirl and cross-tumble flows. Tumble, swirl and cross-tumble ratios (TR, SR and CTR) are calculated as in Eq. 7, 8, 9 and the coordinate system used is illustrated in Figure 10. The instantaneous centre of mass of the gas system is used as reference coordinates $(x_0; y_0; z_0)$, and the normalization to the revving speed allows an objective comparison of flow structures intensity at different engine speeds.

$$TR = \frac{1}{2\pi n} \cdot \frac{\sum_i m_i[(z_i-z_0)u_i-(x_i-x_0)w_i]}{\sum_i m_i(|x_i-x_0|^2+|z_i-z_0|^2)} \qquad \text{(Eq. 7)}$$

$$SR = \frac{1}{2\pi n} \cdot \frac{\sum_i m_i[(x_i-x_0)v_i-(y_i-y_0)w_i]}{\sum_i m_i(|x_i-x_0|^2+|y_i-y_0|^2)} \qquad \text{(Eq. 8)}$$

$$CTR = \frac{1}{2\pi n} \cdot \frac{\sum_i m_i[(y_i-y_0)w_i-(z_i-z_0)v_i]}{\sum_i m_i(|y_i-y_0|^2+|z_i-z_0|^2)} \qquad \text{(Eq. 9)}$$

As for Engine 1, the 2-valve layout with valve axes aligned to the cylinder axis suppresses the formation of an intense tumble flow, while the asymmetric port configuration induces a weak clockwise-oriented (referring to Figure 10) swirling motion. The flow motion generated during the intake stroke and the absence of a dominating tumble structure is shown in Figure 11 (top) for a representative cycle. A good correlation with swirl structure ($\rho_{Swirl\text{-}MFB1}$=-0.29) is found with the CCV of MFB1, together with a weak contribution of tumble (undirected ports layout, $\rho_{Tumble\text{-}MFB1}$=0.18) and with almost null relationship with cross-tumble ($\rho_{Cross\text{-}Tumble\text{-}MFB1}$=-0.003). As for Engine 2, the high-revving condition combined with the oriented intake ports promotes the formation of an intense tumbling motion. This is visible in Figure 11 (bottom), where the more intense flow compared to Engine 1 can be appreciated by the higher scale range. This is confirmed by a good correlation between MFB1 variability and tumble ($\rho_{Tumble\text{-}MFB1}$=-0.25) as well as with swirl ($\rho_{Swirl\text{-}MFB1}$=-0.19), while again cross-tumble does not play a role on combustion instability ($\rho_{cross\text{-}Tumble\text{-}MFB1}$=-0.08).

In conclusion, in the low-turbulent/low-revving condition of Engine 1 none of the considered global thermodynamic variables plays a remarkable role in the variability of MFB1, while for the high-revving Engine 2 the in-cylinder pressure, trapped fuel and tumble ratio have a comparable yet relatively modest weight. In both engines the tumble and swirl flow structures are found to impact moderately on early combustion CCV.
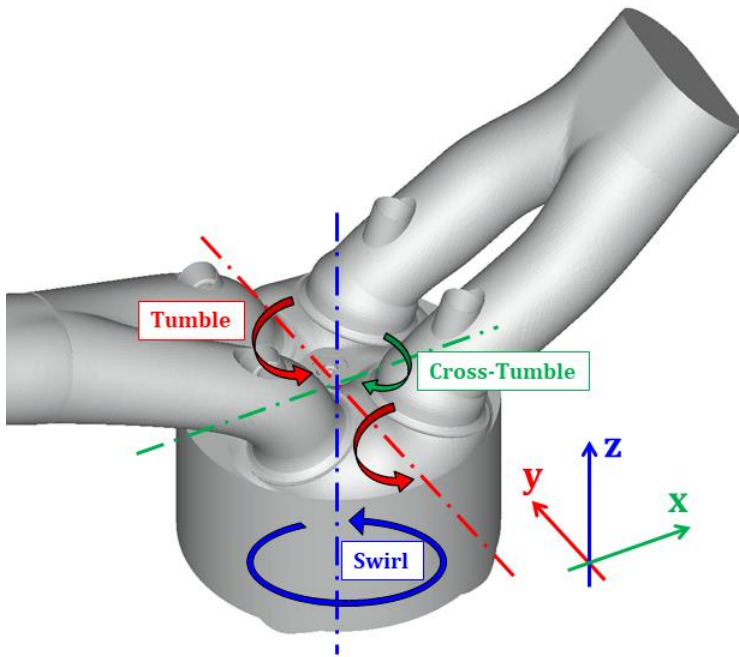
Figure 10. Coordinate systems used for the definition of tumble (red), swirl (blue) and cross-tumble (green). The same convention is used for Engine 1 and 2.
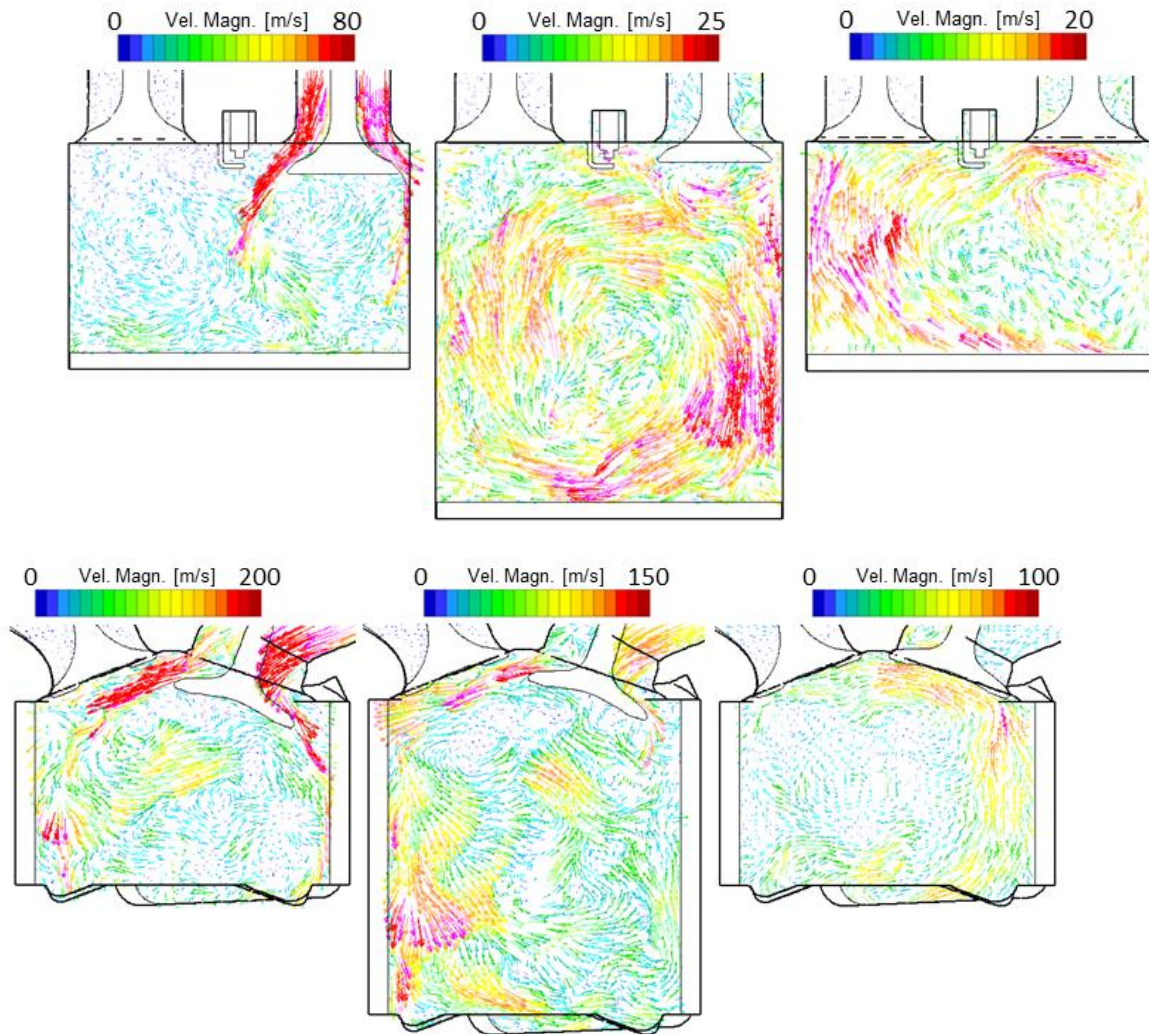
Figure 11. Resolved flow field at 450 CA (left), 540 CA (middle) and 630 CA (right) of a LES representative cycle on a section plane containing intake valve axis. The vector length is proportional to the field magnitude: Engine 1 (top) and Engine 2 (bottom).

Analysis of Local Spark-Plug Variables on Combustion Variability

The analysis focuses then on local mixture and flow-related features at ignition timing (i.e. 18/12 CA bTDC for Engine 1/2) in the spark-plug region (5 mm radius spherical region, centered in the ignition point for both engines). The distributions of the resolved velocity components are reported for Engine 1 and Engine 2 in Figure 12. Differences in engine layout (e.g. port orientation) and revving speed lead to relevant discrepancies in velocity magnitude and distributions. As for Engine 1, the u/w-components of the filtered velocity (i.e. the ones related to tumble motion) show mean values close to zero, with high probability to have both positive and negative u/w-velocities: this depicts randomly oriented local flow for flame kernel growth, strongly exposed to cyclic variability. A similar situation is also observed for v-component at spark plug. Engine 2 presents a very different scenario for u/w-velocity components, with a dominant flow oriented towards the exhaust side of the combustion chamber (i.e. $\langle \bar{u} \rangle < 0$, $\langle \bar{w} \rangle > 0$). The amplitude of the u/v/w-velocity distributions reveals intensities one order of magnitude higher than those for Engine 1.

This situation is confirmed in Figure 13 by the velocity polar plots of u/w and u/v-components at ignition timing, i.e. those related to tumble and swirl structures, respectively. Vectors are the spatial average of the filtered velocity components at ignition time in the spherical region of interest. In Engine 1 the enflamed

14

flame kernel experiences a stochastically oriented flow in both planes, as represented by the randomly-oriented velocity vectors on both u-v and u-w planes, while in Engine 2 a dominant flow direction towards the exhaust side of the combustion chamber is clearly observed. The distributions of Equivalence Ratio and EGR dilution rate are reported in Figure 14: a stoichiometric mixture diluted by burnt products residuals is present in Engine 1 at ignition, while the incomplete homogenization of fuel/air mixture in Engine 2 is responsible for important variability of flammable mixture characteristics (e.g. laminar flame speed).
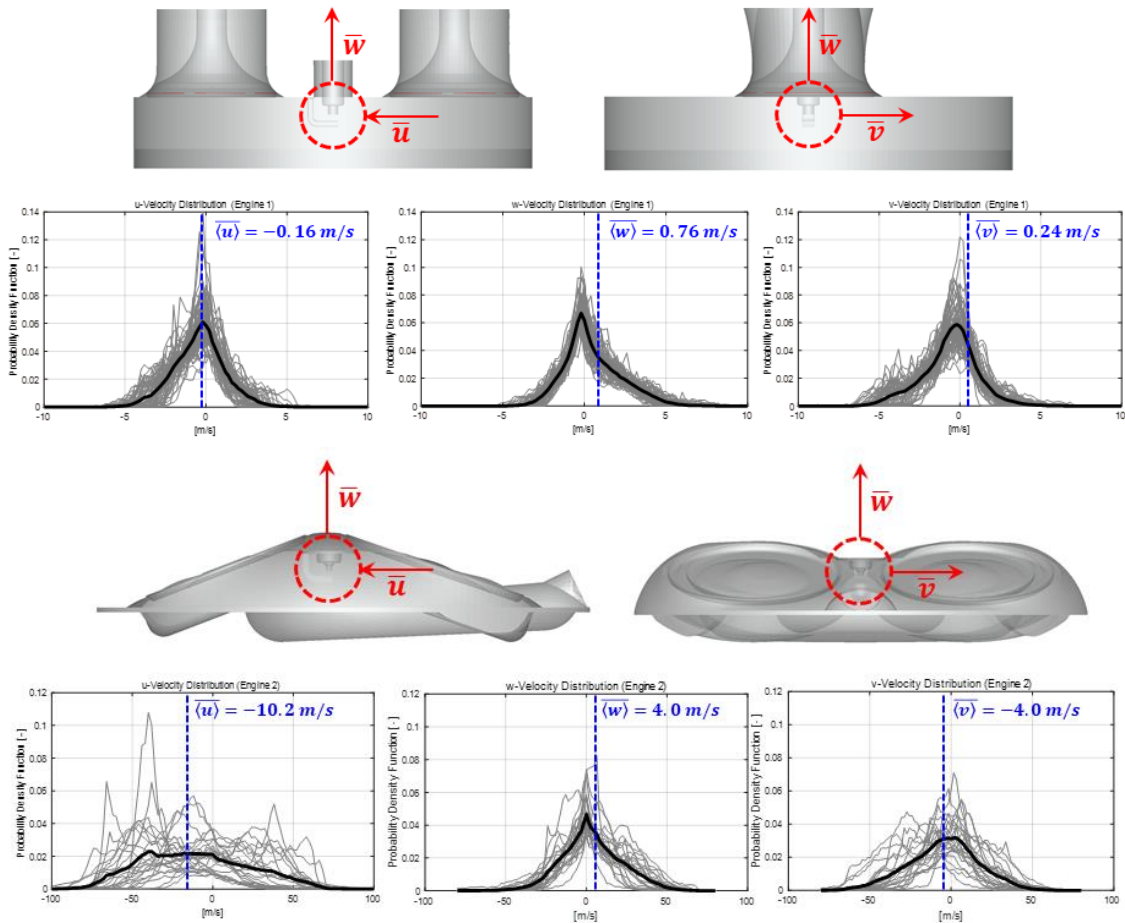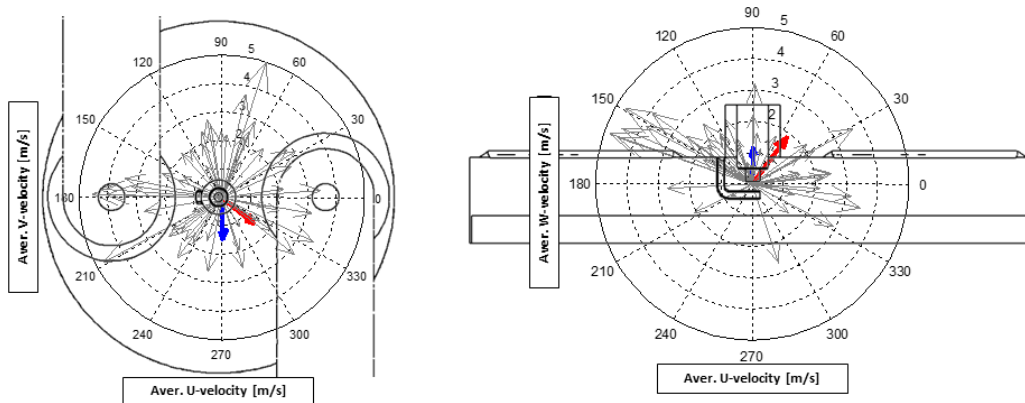

Figure 12. Distribution of filtered $\langle \overline{u} \rangle$, $\langle w \rangle$, $\langle v \rangle$ velocities for the 60 cycle of Engine 1 (60 cycles, top part) and Engine 2(23 cycles, bottom part): cycle-resolved distributions (thin grey) and ensemble average (thick black) are reported.
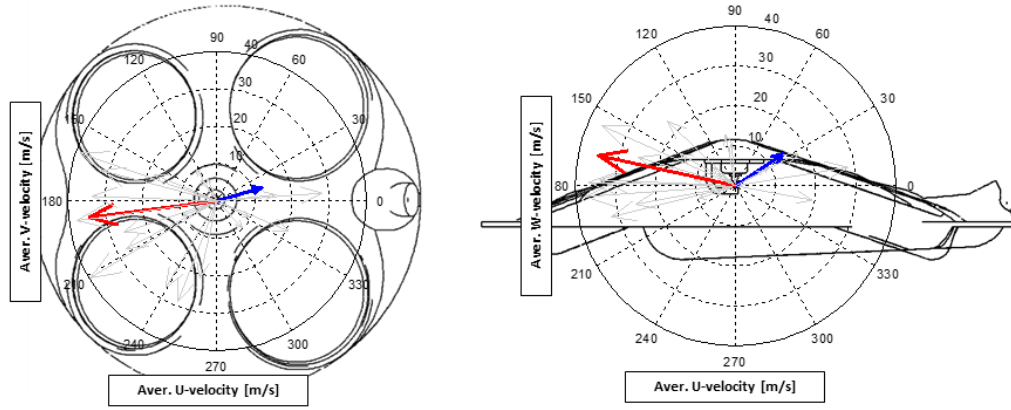
Figure 13. Polar plots of spatially-average velocity components in the ignition region for Engine 1 (60 cycles, top part) and Engine 2 (23 cycles, bottom part): cycle-resolved velocities (thin grey) and fastest/slowest burning cycles (red and blue) are reported. The vector length is proportional to the velocity magnitude.
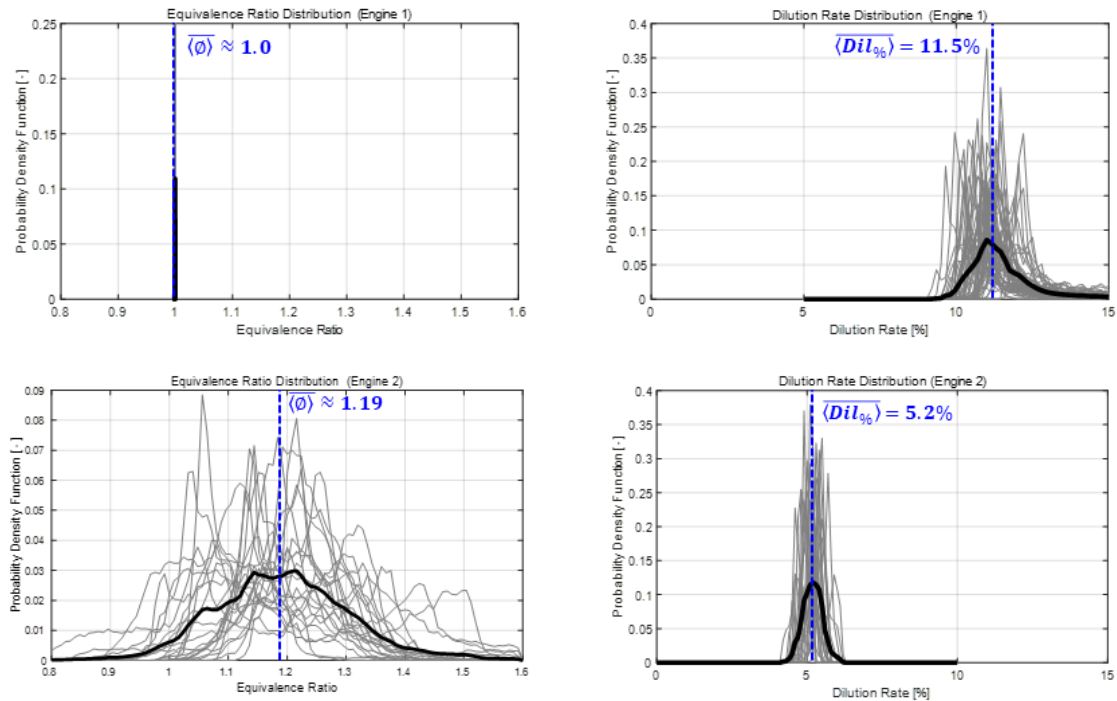

Figure 14. Distribution of filtered Equivalence Ratio and Dilution Rate for Engine 1 (60 cycle, top part) and Engine 2 (23 cycles, bottom part): cycle-resolved distributions (thin grey) and ensemble average (thick black) are reported.

MFB1 is then correlated to the magnitude of the resolved flow field and the AFR at spark; their impact is reported in Figure 15. In Engine 1, values as low as $\rho_{VelSpark-MFB1}$=-0.14 and $\rho_{PhiSpark-MFB1}$=0.07 are found. The former correlation states a weak relationship of MFB1 duration with the resolved velocities at spark time: this is attributed to the weak intensity of the flow fields and to their random orientation.

The latter is expected, as combustion variability of a premixed mixture is almost independent of variability of AFR (the non-null dependence being due to the burnt products dilution). The same analysis on Engine 2 reveals a much stronger impact of both AFR and velocity, with values of $\rho_{VelSpark-MFB1}$=-0.45 and $\rho_{PhiSpark-MFB1}$=0.47. The intensity and orientation of flow structures leads to a close interaction of the growing flame kernel with the local flow field, directly affecting MFB1 duration: cycles with intense flow velocities at ignition present short MFB1 durations (i.e. negative correlation) and rapid flame kernel development. As for mixture quality, the partially-premixed fuel-enriched operation of Engine 2 implies a relevant dependence on AFR at ignition: cycles with closer-to-stoichiometric mixture (i.e. lower Equivalence Ratio) will develop a faster burn rate (i.e. low MFB1) than those with excessively fuel-enriched mixture.
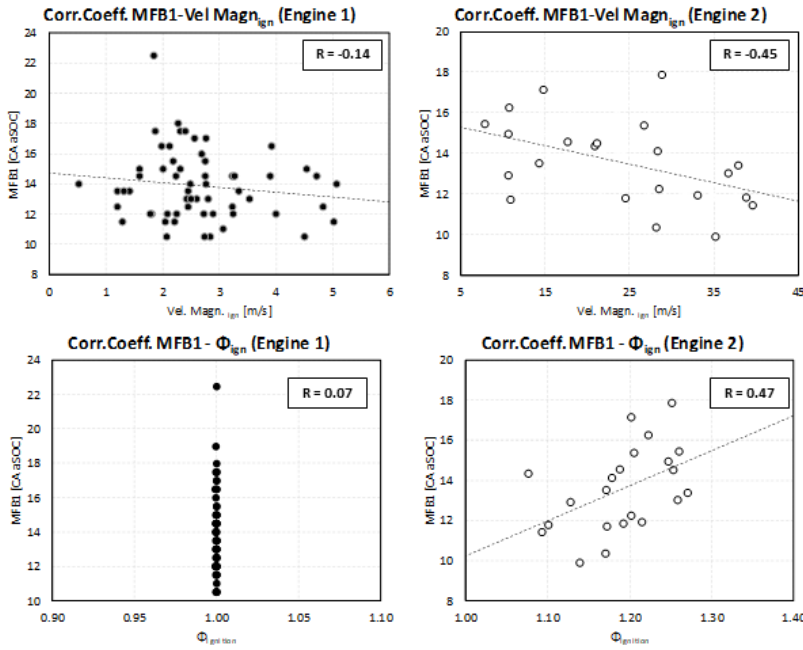
Figure 15. Correlation analysis between velocity magnitude (top row)/equivalence ratio (bottom row) at ignition and MFB1 combustion duration for Engine 1 (left side) and Engine 2 (right side).

Comprehensive results for the identification of leading factors for MFB1 cyclic variability are summarised in Figure 16, where all the calculated correlation coefficients are compared for Engine 1 and 2. The many differences between the two units lead to engine-specific weights of each factor on combustion CCV. As for Engine 1, the only emerging factors are related to large-scale flow structures, i.e. tumble/swirling motions: despite their low absolute intensity and considering the comparable weight of multiple factors (e.g. the absence of preferential flow orientation at ignition and the high cyclic repeatability of thermodynamics conditions), they are the strongest contributors to MFB1 fluctuation. Engine 2 is less stable in terms of thermodynamics conditions: a more intense tumble flow is promoted and the direct-injection fuel-rich operation in conjunction with the high-revving operation causes cyclic fluctuation of AFR in the spark plug proximity. For this reason, Engine 2 moderately benefits of an intense TR to support a fast combustion onset (i.e. short MFB1), although the dominant factor is the local U-vel. component, differently from the more chaotic flow condition present in Engine 1 at ignition (see Figure 13).
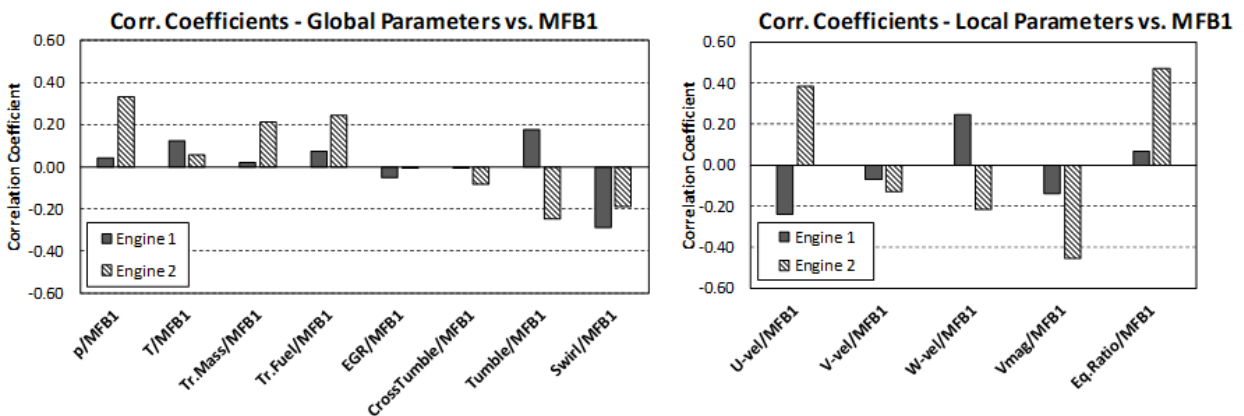
Figure 16. Correlation coefficients between global (left)/local (right) variables and MFB1 combustion durations for Engine 1 (filled bars) and Engine 2 (dashed bars).

***Figure 17.** **Isosurface for $\tilde{c} = 0.5$ (1ˢᵗ row), filtered flow and flame isolines in the range of $\tilde{c} = 0.15 - 0.5$ on two orthogonal section planes (2ⁿᵈ and 4ᵗʰ row) and $\tilde{c} \cdot (1 - \tilde{c})$ contour plot (3ʳᵈ row) in Engine 1: slow-burning (top part) and fast-burning (fast-burning) cycle.*

Figure 18. *Isosurface for $\tilde{c} = 0.5$ (1st row), filtered flow and flame isolines in the range of $\tilde{c} = 0.15 - 0.5$ on two orthogonal section planes (2nd and 4th row) and $\tilde{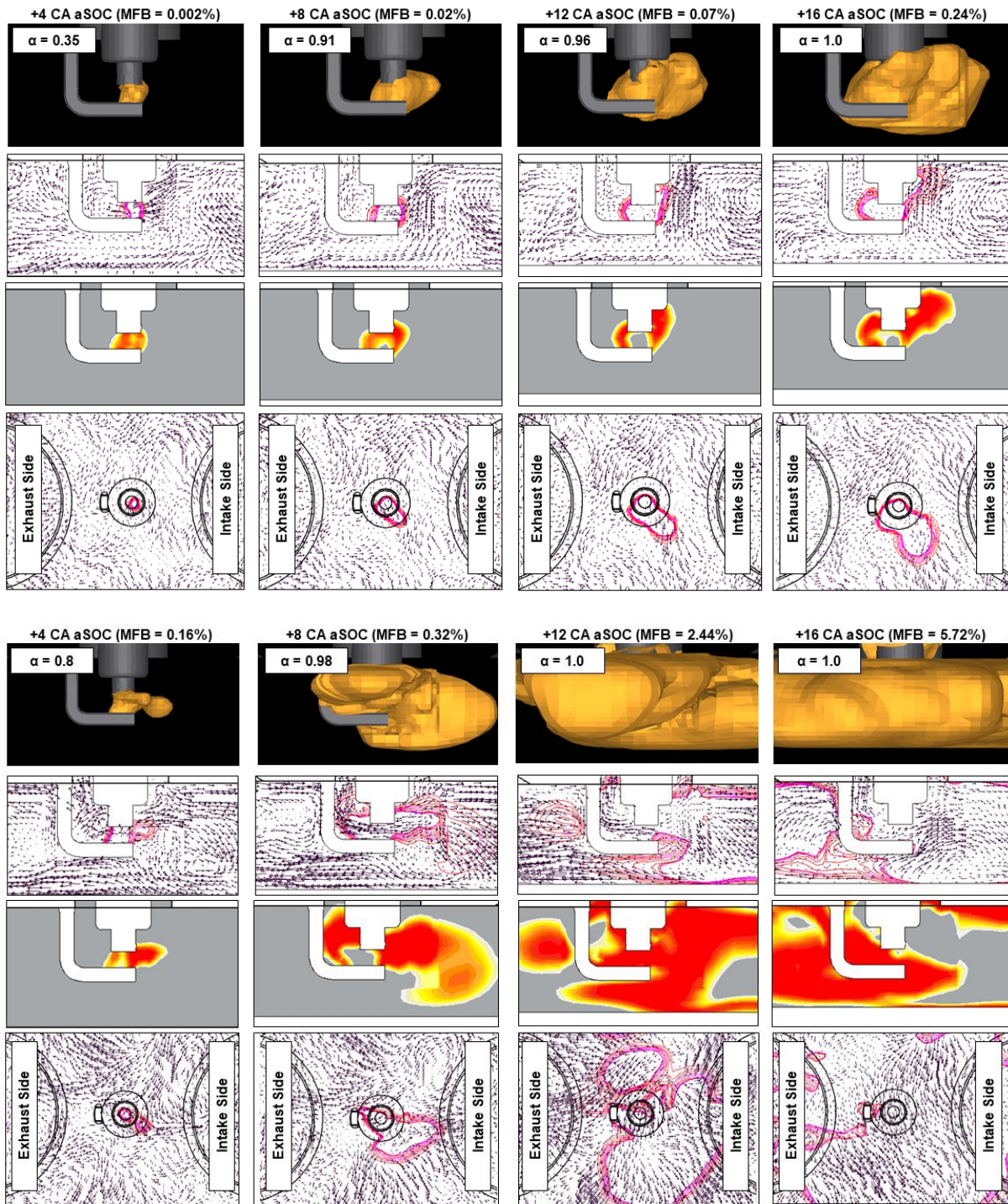c} \cdot (1 - \tilde{c})$ contour plot (3rd row) in Engine 2: slow-burning (top part) and fast-burning (fast-burning) cycle.*
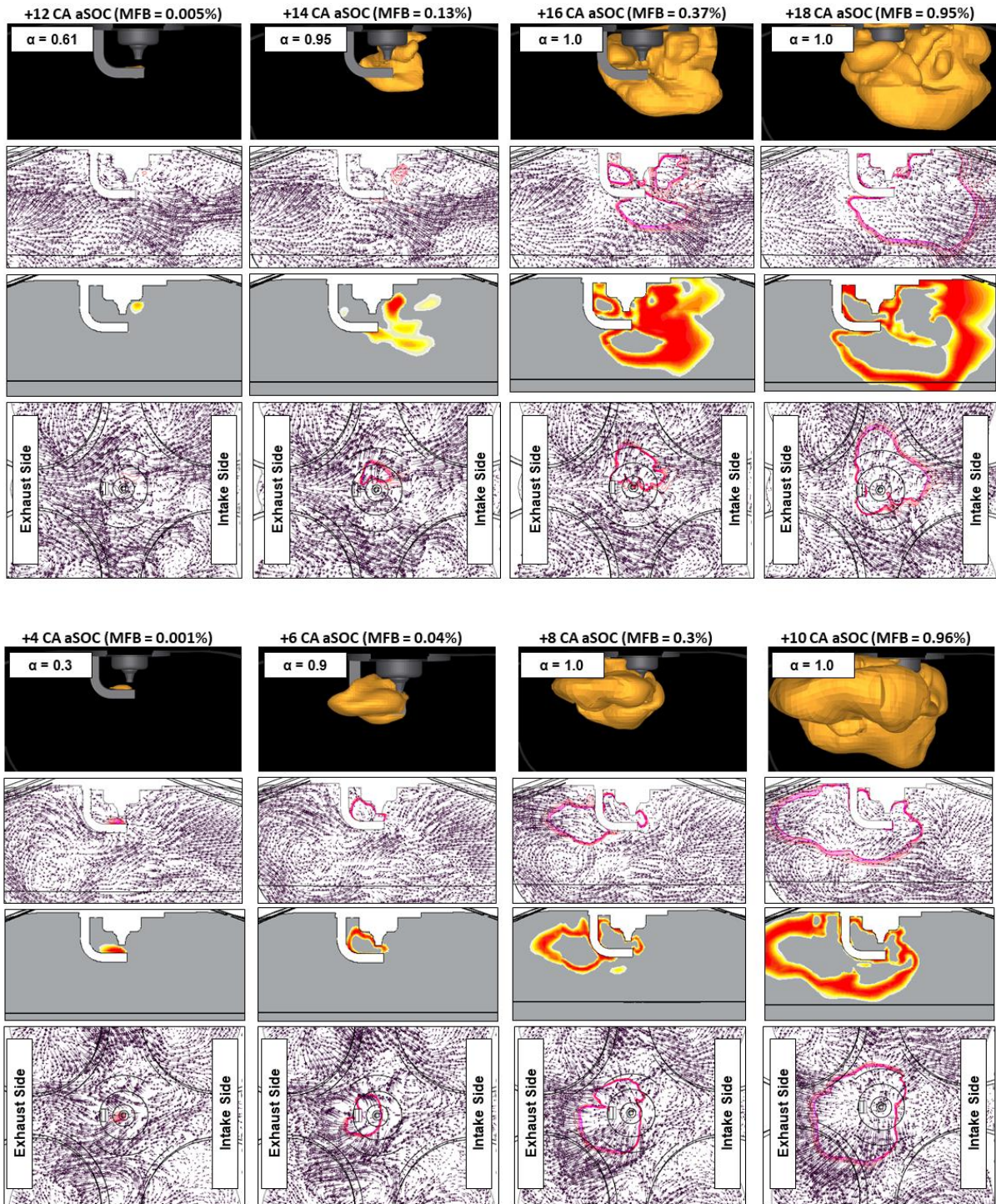
Finally, the flame kernel development for the extreme cycles of both engines are illustrated in Figures 17-18. Cycles with the maximum/minimum pressure peaks are selected as representative of slow/fast-burning cycles. The ISSIM-LES ignition model accounts for the interaction between flame and local flow details, whose mean velocities are illustrated in the polar plots in Figure 13 as blue (slow-burning) and red (fast-burning) vectors. As for Engine 1 both the slowest and the fastest cycle show a flame kernel development centered around the spark plug, as a consequence of the low-intensity and randomly-oriented flow field. In Engine 2 the flame in the selected fast-burning cycle grows towards the exhaust side, due to an intensely tumbling flow, whereas the slow-burning cycle experiences a side-oriented flow at ignition, leading to a delayed flame growth.

The different outcomes from Engine 1 and 2 confirm the impossibility to outline a general ranking of CCV causes valid for any S.I. engine. A similar analysis of flame topology and interaction with the flow field was conducted by Zhao et al. [64], although under a different load and revving speed (2500 rpm): authors found that fast-burning cycles were governed by low tumble velocities, confirming the validity of the study findings limited to the analyzed engine. In this context, the use of models able to simulate the flame kernel interaction with the local flow nature is essential to allow Large-Eddy Simulation to fill an area where experiments solely based on engine pressure would be hardly explanatory.

Effect of Simple Ignition Models on Combustion CCV

To further emphasize the importance of models able to simulate the flame evolution since the initial stage (ISSIM-LES in this study) a comparison with a simpler ignition model is presented hereafter; also, the impact of model assumptions will be pointed out. The previously presented combustion events are repeated for the two engines using a simpler flame-deposition model (FD), this being the only variation in the CFD setup. This model is based on the imposition of a resolved profile $\tilde{c}$ of burnt gas at ignition timing, following Eq. 10:

$$\tilde{c} = \frac{c_0}{2} \cdot \left(1 - tanh\frac{\|x-x_{spk}\|}{r_k}\right)$$

(Eq. 10)

In Eq. 10 the laminar flame kernel radius is calculated as $r_k = 15\delta_L \, {T_b}/{T_u}$ (with T_b and T_u the burnt and unburnt temperature and δ_L the laminar flame thickness), and c_0 is a model constant ($c_0 = 4$ here). In order to compensate for the absence of dedicated terms to ignition, a resolved spherical flame kernel is imposed, with no model of the secondary electric circuit. Flow realizations at spark-timing presented earlier are used as initial conditions for each Engine: this ensures that the new combustion simulations develop in the same flow/mixture environment as those of the ISSIM-LES cases (i.e. same PDFs of velocity/AFR at ignition, etc.). The simulation results for both Engine 1 and 2 are reported in Figure 19.
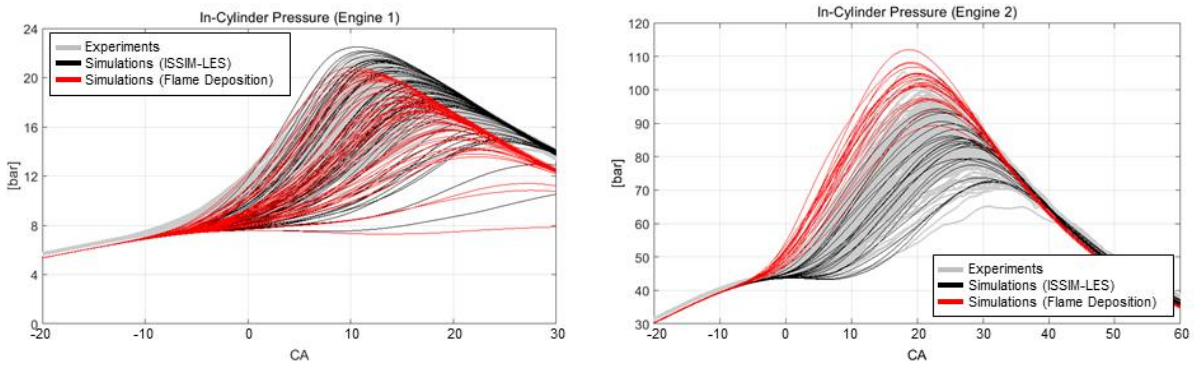
Figure 19. Combustion pressure traces from simulations using a Flame Deposition (red) and ISSIM-LES (black) ignition model, and experiments (grey): Engine 1 (left) and Engine 2 (right).

Due to the lack of a proper treatment of subgrid-scale flame kernel, the ignition model prescribes an immediately resolved flame size ($r_k \approx 0.5 \, mm$). A first consequence is combustion phasing, as the initial flame lifetime is not simulated and combustion is anticipated compared to the experiments: although a dedicated tuning of the ignition phase (e.g. delaying the flame deposition timing) may improve the results, this is not advisable in a simulation study aiming at reducing the modelling assumptions. A second effect is in the resulting combustion CCV, which is altered by the imposition in the flow of a resolved-size self-similar burnt profile.

The average peak pressure is not relevantly altered in Engine 1 by the use of a simpler ignition model, whereas in Engine 2 the band of pressure cycles substantially moves towards the upper band of experimental cycles (Figure 20). As for cyclic variation, the agreement of the simulated combustion CCV with respect to ISSIM-LES worsens for both Engine 1 and 2 (Figure 20).
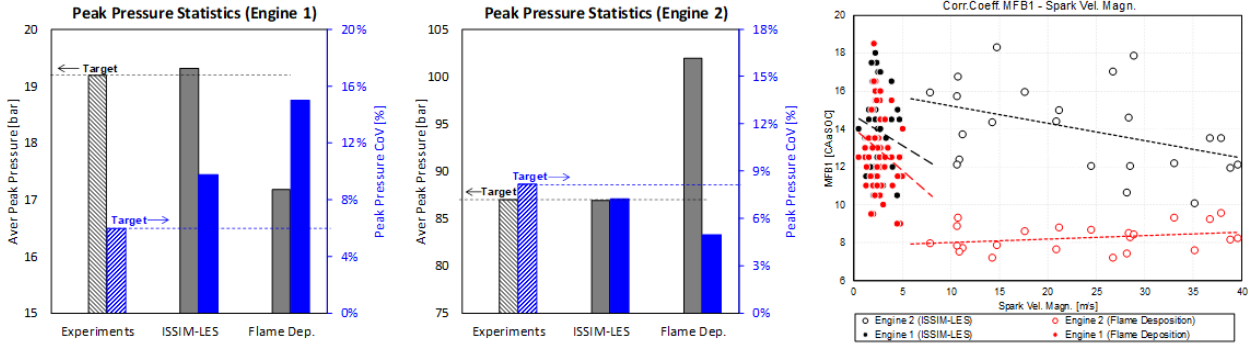

Figure 20. Average (grey) and CoV (blue) of peak pressure for experiments and simulations (ISSIM-LES and Flame Deposition): Engine 1 (left) and Engine 2 (middle). Correlation analysis between local velocity at ignition and MFB combustion duration (right) for ISSIM-LES (black symbols) and Flame Deposition (red symbols) models: Engine 1 (filled symbols) and Engine 2 (empty symbols).

The correlation between the local velocity magnitude and MFB1 for the two ignition models is reported in Figure 18. As for Engine 1, the relationship with local flow velocity and MFB1 is not relevantly different using either ISSIM-LES or FD ignition model ($\rho_{vmag-MFB1(ISSIM-LES)}$=-0.14 and $\rho_{vmag-MFB1(FD)}$=-0.18). The same holds for the equivalence ratio, with $\rho_{\Phi-MFB1(ISSIM-LES)}$=0.07 and $\rho_{\Phi-MFB1(FD)}$=-0.02. The absence of a close relationship between the CCV of the flow velocity/orientation or local AFR and the MFB1 duration observed for the ISSIM-LES simulations states the contribution of many interplaying factors with similar weight in the CCV of MFB1: in this context, the use of a simpler FD ignition model has a limited impact on combustion CCV.

In Engine 2 the use of the FD ignition model would lead to a different interaction between flame and local flow, therefore affecting the simulated combustion CCV. The correlation between the local flow velocity and the early combustion duration is reversed, with $\rho_{vmag-MFB1(ISSIM-LES)}$=-0.45 and $\rho_{vmag-MFB1(FD)}$=0.27: this leads to the unrealistic result of cycles subjected to low-velocity flow at spark being those with faster burn rate (i.e. low MFB1). This aspect is particularly critical in Engine 2, given the higher flow velocities at ignition with respect to Engine 1: the use of an advanced ignition model in this application is fundamental for a correct simulation of combustion CCV. Finally, the correlation between mixture quality at spark and early combustion duration on Engine 2 is poorly influenced by the use of a FD ignition model ($\rho_{\Phi-MFB1(ISSIM-LES)}$=0.47 and $\rho_{\Phi-MFB1(FD)}$=0.45), leaving the most critical aspect to the flow velocity/flame interaction.

Conclusions

This study shows the capability of modern LES simulations to quantitatively reproduce combustion CCV in two different S.I. engines and to establish a ranking of CCV promoting factors. Well-established models for combustion and turbulence are adopted, in conjunction with a recently-developed spark-ignition model (ISSIM-LES) allowing the simulation of flame/flow interaction since the early flame nucleus appearance; this target is accomplished thanks to the resolution of a FSD-LES equation modified to account for subgrid-scale flame stretch for small-radius flame (i.e. comparable to the cell size); a function of the flame radius governs a smooth transition between ignition and propagation phase, recovering the standard FSD-LES equation. This modelling framework allows a detailed understanding of the root causes for combustion events variability of two very different S.I. units: the Transparent Combustion Chamber (TCC) research

engine and a modern GDI turbocharged V8 unit (Engine 1 and 2). The comparison with experimentally measured pressure traces in firing conditions confirms the ability of LES simulations to globally reproduce the measured combustion variability for both units, although some excessively slow-burning cycles are present for Engine 1.

A very high correlation between the early combustion duration (MFB1) and the combustion peak pressure is found for both units using common metrics as in the experiments, i.e. pressure-based analysis of heat release rate. Therefore, simulations are used to shed a light on the role of large and small-scale factors on early combustion development:

- As for large-scale factors, in-cylinder pressure, trapped fuel and tumble ratio are relevant CCV-originating factors only in Engine 2 (high-tumble/high-revving operation), whereas large-scale flow structures (tumble and swirl) differently affect combustion CCV in the two units;
- Moving to small-scale factors, observations are taken on a small volume surrounding the spark plug. The premixed operation of Engine 1 and the absence of intense coherent flow structures leads to a similarly-mixed AFR and random flow fields: a comparable weight is calculated for all the factors, preventing the identification of few dominant factors originating combustion CCV. On the contrary, Engine 2 experiences a high-velocity ignition regime, and the DI operation causes a stratified fuel-rich gasoline/air mixture at ignition. Both velocity magnitude and AFR in the spark plug proximity emerge as main responsible for the variability of 1% burn duration, hence affecting the whole combustion history.

Finally, simulations are repeated using a simpler Flame Deposition ignition model, with the aim of highlighting the improved simulation capability of the ISSIM-LES ignition model used in the first part. The same sets of flow realizations are used for the two engines, so that combustion develops using initial conditions identical to the first set of simulations. Results show a reduced benefit from the use of an advanced ignition model in Engine 1, mainly due to the low flow velocities at ignition and the reduced variability of mixture composition. Conversely, in Engine 2 the intense flow velocity originated by the high-tumble/high-revving operation emphasizes the benefit from using a fully-coupled flame/flow ignition model (ISSIM-LES) rather than a rigidly imposed self-similar initial burnt profile. Also, the simulated combustion CCV is in good agreement with the experiments using ISSIM-LES, while it halves the value using the FD ignition model.

This study demonstrates that the use of LES and advanced ignition models can be used to well reproduce the measured combustion CCV in two very different S.I. engines exhibiting different flow/mixture conditions at ignition. A clear identification and ranking of CCV responsible factors is made possible thanks to reduced modelling assumptions present in the adopted ignition model. The maturity of LES simulations to explain turbulence-generated phenomena causing combustion instability in S.I. engines is proved, and the different conclusions for the two analyzed cases confirm the impossibility to draw a general framework valid for all types of S.I. units. In this context the use of LES simulations emerges as an unprecedented tool to outline new design perspectives and development directions for next-generation ICE.

Acknowledgements

Nomenclature

AFR	Air-to-Fuel Ratio
aMFB	Apparent Mass Fraction Burnt
aSOC	After Start of Combustion
CCV	Cycle-to-Cycle Variation
CHR	Cumulative Heat Release
CoV	Coefficient of Variation
CTR	Cross-Tumble Ratio
EGR	Exhaust Gas Recirculation
ER	Energy Resolution
FD	Flame Deposition
FSD	Flame Surface Density
GDI	Gasoline Direct Injection
ICE	Internal Combustion Engine
LES	Large-Eddy Simulation
LFS	Laminar Flame Speed
MAP	Manifold Absolute Pressure
MFB	Mass Fraction Burnt
PDF	Probability Density Function
ROHR	Rate of Heat Release
S.I.	Spark-Ignition
SR	Swirl Ratio
TCC	Transparent Combustion Chamber
TR	Tumble Ratio

References

1. Ozdor, N., Dulger, M. and Sher, E. (1994) Cyclic variability in spark ignition engines: A literature survey, SAE Technical Paper 940987.
2. Young, M., "Cyclic Dispersion in the Homogeneous-Charge Spark-Ignition Engine—A Literature Survey," SAE Technical Paper 810020, 1981, doi:10.4271/810020.
3. Finney, C.E.A., et al. "Invited review: a review of deterministic effects in cyclic variability of internal combustion engines." International Journal of Engine Research 16.3 (2015): 366-378.
4. Rutland, C. J., "Large-eddy simulations for internal combustion engines- A review", International Journal of Engine Research, vol. 12, no. 5, pp. 421-451, 2011 doi: 10.1177/1468087411407248.
5. Haworth, D.C., "Large-Eddy Simulation of In-Cylinder Flows", Oil & Gas Science and Technology Ð Rev. IFP, Vol. 54 (1999), No. 2, pp. 175-185
6. Smagorinsky J., "General circulation experiments with the primitive equations," Mon. Wea. Rev. 91, 99-164.
7. Pomraning, E., Rutland, C.J., "Dynamic One-equation Nonviscosity Large-Eddy Simulation Model", AIAA Journal, Vol.40, No.4, April 2002
8. Piscaglia, F., Montorfano, A., Onorati, A., Brusiani, F., "Boundary Conditions and SGS Models for LES of Wall-Bounded Separated Flows: An Application to Engine-Like Geometries", Oil & Gas Science and Technology – Rev. IFP Energies nouvelles, DOI: 10.2516/ogst/2013143
9. Ko, I., D'Adamo, A., Fontanesi, S., and Min, K., "Study of LES Quality Criteria in a Motored Internal Combustion Engine," SAE Technical Paper 2017-01-0549, 2017, doi:10.4271/2017-01-0549
10. Ko, I., Min, K., Rulli, F., D'Adamo, A. et al., "Investigation of Sub-Grid Model Effect on the Accuracy of In-Cylinder LES of the TCC Engine under Motored Conditions," SAE Technical Paper 2017-24-0040, 2017.

11. Abraham, K. Liu, D. Haworth, D. Reuss and V. Sick, "Evaluating Large-Eddy Simulation (LES) and High-Speed Particle Image Velocimetry (PIV) with Phase-Invariant Proper Orthogonal Decomposition (POD)", Oil & Gas Science and Technology – Rev. IFP Energies nouvelles, Vol. 69 (2014), No. 1, pp. 3-188

12. Yang, X., Gupta, S., Kuo, T-W., Gopalakrishnan, V., "RANS and Large Eddy Simulation of Internal Combustion Engine Flows—A Comparative Study", Journal of Engineering for Gas Turbines and Power, MAY 2014, Vol. 136

13. Kuo, T-W, Yang, X., Gopalakrishnan, V., Chen, Z., "Large Eddy Simulation (LES) for IC Engine Flows", Oil & Gas Science and Technology – Rev. IFP Energies nouvelles, 10.2516/ogst/2013127

14. Goryntsev, D., Sadiki, A., Klein, M. and Janicka, J. (2009) Large eddy simulation based analysis of the effects of cycle-to-cycle variations on air–fuel mixing in realistic DISI IC-engines, Proc. Combust. Inst., 32:2759-2766.

15. Goryntsev, D., Sadiki, A. and Janicka, J. (2013) Analysis of misfire processes in realistic direct injection spark ignition engine using multi-cycle large eddy simulation, Proc. Combust. Inst., 34:2969-2976.

16. Janas, P., Wlokas, I., Böhm, B., Kempf, A., "On the Evolution of the Flow Field in a Spark Ignition Engine", Flow Turbulence Combust, DOI 10.1007/s10494-016-9744-3

17. Buhl, S., "Scale-resolving simulations of internal combustion engine flows", PhD Thesis

18. Nguyen, T., Janas, P., Lucchini, T., D'Errico, G. et al., "LES of Flow Processes in an SI Engine Using Two Approaches: OpenFoam and PsiPhi," SAE Technical Paper 2014-01-1121, 2014, https://doi.org/10.4271/2014-01-1121.

19. Johansson, B. (1996) Cycle to cycle variations in S.I. engines - The effects of fluid flow and Gas composition in the vicinity of the spark plug on early combustion, SAE Technical Paper 962084.

20. Reuss, D.L. (2000) Cyclic variability of large-scale turbulent structures in directed and undirected IC engine flows, SAE Technical Paper 2000-01-0246.

21. Aleiferis, P., Taylor, A., Whitelaw, J., Ishii, K. et al., "Cyclic Variations of Initial Flame Kernel Growth in a Honda VTEC-E Lean-Burn Spark-Ignition Engine," SAE Technical Paper 2000-01-1207, 2000, https://doi.org/10.4271/2000-01-1207.

22. Wei, H., Zhu, T., Shu, G., Tan, L., Wang, Y., "Gasoline engine eaxhaust gas recirculation – a review", Applied Energy 2012;99:534-544

23. Pera, C., Knop, V. and Reveillon, J. (2015) Influence of flow and ignition fluctuations on cycle-to-cycle variations in early flame kernel growth, Proc. Combust. Inst., 35:2897-2905.

24. Granet, V., Vermorel, O., Lacour, C., Enaux, B., Dugué, V. and Poinsot, T. (2012) Large-eddy simulation and experimental study of cycle-to-cycle variations of stable and unstable operating points in a spark ignition engine, Combust. Flame, 159:1562-1575.

25. Truffin, K., Angelberger, C., Richard, S. and Pera, C. (2015) Using large-eddy simulation and multivariate analysis to understand the sources of combustion cyclic variability in a spark-ignition engine, Combust. Flame, 162(12):4371-4390.

26. Adomeit, P., Lang, O., Pischinger, S., Aymanns, R. et al., "Analysis of Cyclic Fluctuations of Charge Motion and Mixture Formation in a DISI Engine in Stratified Operation," SAE Technical Paper 2007-01-1412, 2007

27. Colin, O. and Truffin, K. (2011) A spark ignition model for large eddy simulation based on an FSD transport equation (ISSIM-LES), Proc. Combust. Inst., 33:3097-3104.

28. Robert, A., Richard, S., Colin, O., Martinez, L., De Francqueville, L., "LES prediciton and analysis of knocking combustion in a spark ignition engine", Proc. Comb. Inst. 35 (2015) 2941-2948

29. Pan, J., Wei, H., Shu, G., Pan, M., Feng, D., Li, N., « LES analysis for auto-ignition induced abnormal combustion based on a downsized SI engine », Applied Energy 191 (2017) 183-192

30. Fontanesi, S., d'Adamo, A., Rutland, C.J., "Large-Eddy simulation analysis of spark configuration effect on cycle-to-cycle variability of combustion and knock," International Journal of Engine Research, April 2015; vol. 16, 3: pp. 403-418., first published on January 9, 2015.

31. d'Adamo, A., Breda, S., Fontanesi, S. and Cantore, G. "LES Modelling of spark-ignition cycle-to-cycle variability on a highly downsized DISI engine", *SAE Intern'l. J. Engines,* 8:2029-2041.

32. d'Adamo, A., Ph.D. Thesis, "Numerical Modelling of Abnormal Combustion Events in High-Performance Spark-Ignition Engines, University of Modena and Reggio Emilia (2015).

33. d'Adamo, A., Breda, S., Cantore, G., "Large-eddy simulation of cycle-resolved knock in a turbocharged SI engine", Energy Procedia Volume 82, 2015, Pages 45-50

34. Y. Shekhawat, D.C. Haworth, A. d'Adamo, F. Berni, S. Fontanesi, P. Schiffmann, D.L. Reuss and V. Sick, "An Experimental and Simulation Study of Early Flame Development in a Homogeneous-charge Spark-Ignition Engine"; Oil & Gas Science and Technology - Rev. IFP Energies nouvelles (2017) 72, 32.

35. Vermorel, O., Richard, S., Colin, O., Angelberger, C., Benkenida, A., Veynante, D., "Towards the understanding of cyclic variability in a spark ignited engine using multi-cycle LES," Combust. Flame 156, 8, 1525-1541 (2009).

36. Richard S., Colin O., Vermorel O., Benkenida A., Angelberger C., Veynante D. (2007) Towards large eddy simulation of combustion in spark ignition engines Proc. Combust. Inst. 31, 3059-3066.

37. Colin, O., Ducros, F., Veynante, D., Poinsot, T., "A thickened flame model for large-eddy simulations of turbulent premixed combustion", Physics of Fluids, Vol.12, Number 7

38. Shekhawat, Y. (2016) Large-Eddy Simulations of Flow and Combustion in Spark-Ignition Engines. Ph.D. thesis, The Pennsylvania State University, University Park, PA, U.S.A.

39. Schiffmann, P. (2016) Root Causes of Cycle-to-Cycle Combustion Variations in Spark Ignited Engines. Ph.D. thesis, University of Michigan, Ann Arbor, MI, U.S.A.

40. Sick, V., Reuss, D.L., Yang, X. and Kuo, T.-W. (2014) https://deepblue.lib.umich.edu/handle/2027.42/108382

41. Vafamehr, H., Cairns, A., Sampson, O., Moslemin Koupaie, M., "The competeing chemical and physical effects of transient fuel enrichment on heavy knock in an optical spark-ignition engine", Applied Energy 179 (2016), 687-697

42. Di Mare, F., Knappstein, R., Baumann, M., "Application of LES-quality criteria to internal combustion engine flows," Computers & Fluids 89 (2014) 200–213

43. Fontanesi, S., Paltrinieri, S., D'Adamo, A. and Duranti, S., "Investigation of Boundary Condition and Field Distribution Effects on the Cycle-to-Cycle Variability of a Turbocharged GDI Engine Using LES," Oil & Gas Science and Technology – Rev. IFP Energies nouvelles, Vol. 69 (2014), No. 1, pp. 107-128 DOI: 10.2516/ogst/2013142.

44. Cicalese, G., Berni, F., and Fontanesi, S., "Integrated In-Cylinder / CHT Methodology for the Simulation of the Engine Thermal Field: An Application to High Performance Turbocharged DISI Engines," SAE Int. J. Engines 9(1):601-617, 2016.

45. Cicalese, G., Berni, F., Fontanesi, S., D'Adamo, A. et al., "A Comprehensive CFD-CHT Methodology for the Characterization of a Diesel Engine: from the Heat Transfer Prediction to the Thermal Field Evaluation," SAE Technical Paper 2017-01-2196, 2017.

46. Berni, F., Fontanesi, S., Cicalese, G., and D'Adamo, A., "Critical Aspects on the Use of Thermal Wall Functions in CFD In-Cylinder Simulations of Spark-Ignition Engines," SAE Int. J. Commer. Veh. 10(2):547-561, 2017.

47. Malaguti S, Fontanesi S, Cantore G, Montanaro A and Allocca L. "Modelling of primary breakup process of a gasoline direct engine multi-hole spray," Atomization Spray 2013; 23(10): 861–888 (2013).

48. Breda, S., D'Adamo, A., Fontanesi, S., Giovannoni, N. et al., "CFD Analysis of Combustion and Knock in an Optically Accessible GDI Engine," SAE Int. J. Engines 9(1):641-656, 2016.

49. Breda, S., D'Adamo, A., Fontanesi, S., D'Orrico, F. et al., "Numerical Simulation of Gasoline and n-Butanol Combustion in an Optically Accessible Research Engine," SAE Int. J. Fuels Lubr. 10(1):32-55, 2017.

50. Cavicchi, A., Postrioti, L., Giovannoni, N., Fontanesi, S., Bonandrini, G., Di Gioia, R., "Numerical and experimental analysis of the spray momentum flux measuring on a GDI injector", (2017) Fuel, 206, pp. 614-627

51. Reitz, R., Diwakar, R., "Effect of Drop Breakup on Fuel Sprays", SAE Technical Paper 860469, SAE Trans. 95, 3, 218-227.

52. Duclos J.M., Colin O. (2001) Arc and kernel tracking ignition model for 3D spark-ignition engine calculations, COMODIA, 343-350.

53. Verhoeven D. (1995) Spark heat transfer measurements in flowing gases, SAE Technical Paper 952450.

54. D'Adamo, A., Del Pecchia, M., Breda, S., Berni, F. et al., "Chemistry-Based Laminar Flame Speed Correlations for a Wide Range of Engine Conditions for Iso-Octane, n-Heptane, Toluene and Gasoline Surrogate Fuels," SAE Technical Paper 2017-01-2190, 2017, https://doi.org/10.4271/2017-01-2190.

55. Del Pecchia, M., Breda, S., D'Adamo, A., Fontanesi, S. et al., "Development of Chemistry-Based Laminar Flame Speed Correlation for Part-Load SI Conditions and Validation in a GDI Research Engine," SAE Technical Paper 2018-01-0174, 2018, https://doi.org/10.4271/2018-01-0174.

56. Ranzi, E., Frassoldati, A., Grana, R., Cuoci, A., Faravelli, T., Kelley, A.P., Law, C.K., "Hierarchical and comparative kinetic modeling of laminar flame speeds of hydrocarbon and oxygenated fuels," Progress in Energy and Combustion Science, 38 (4), pp. 468-501 (2012), DOI: 10.1016/j.pecs.2012.03.004

57. Qin, Z., Lissianski, V.V., Yang, H., Gardiner, W., Davis, S.G., Wang, H., "Combustion chemistry of propane: A case study of detailed reaction mechanism optimization," Proceedings of the Combustion Institute, Volume 28, Issue 2, 2000,Pages 1663-1669,ISSN 1540-7489, https://doi.org/10.1016/S0082 0784(00)80565-2.

58. Gauthier, B. M.; Davidson, D. F., Hanson, R. K., "Shock tube determination of ignition delay times in full-blend and surrogate fuel mixtures," Combust Flame 2004, 139, 300–311

59. Andrae, J.C.G., "Development of a detailed kinetic model for gasoline surrogate fuels," Fuel 87 (2008) 2013–2022. 26.

60. Andrae, J.C.G., Head, R.A., "HCCI experiments with gasoline surrogate fuels modeled by a semidetailed chemical kinetic model," Combustion and Flame 156 (2009) 842–851.

61. Ameen, M.M., Mirzaeian, M., Millo, F., Som, S., "Numerical Prediction of Cyclic Variability in a Spark Ignition Engine Using a Parallel Large Eddy Simulation Approach," Journal of Energy Resources Technology, 140(5), 052203.

62. Pope, S.B., "Ten questions concerning the large-eddy simulation of turbulent flows," New Journal of Physics 6 (2004) 35.

63. Ko, I., Min, K., Fontanesi, S., Rulli, F. et al., "Impact of Grid Density on the LES Analysis of Flow CCV: Application to the TCC-III Engine under Motored Conditions," SAE Technical Paper 2018-01-0203, 2018, https://doi.org/10.4271/2018-01-0203.

64. Zhao, Le, et al. "Examining the role of flame topologies and in-cylinder flow fields on cyclic variability in spark-ignited engines using large-eddy simulation." International Journal of Engine Research (2017): 1468087417732447

Appendix

LFS Fit Coefficients	Gasoline (p=20-120 bar)	Propane (p=2-25 bar)
p_0 [bar]	70	25
T_0 [K]	825	1070
a_1	84.6824	209.2508
a_2	42.4108	114.1206
a_3	-292.3464	-374.9285
a_4	-373.1746	-717.1424
a_5	497.2003	-357.7542
a_6	989.9364	629.7534
b_1	2.6325	2.5373
b_2	0.0436	-0.6706
b_3	5.4422	2.9390
b_4	2.1828	5.4509
b_5	-11.6251	15.0293
b_6	-14.3404	17.2323
c_1	-0.3259	-0.3095
c_2	-0.1949	0.1366
c_3	-0.5918	-0.3113
c_4	1.4440	-0.9263
c_5	2.7850	-1.2143
c_6	-0.2560	0.3896